Textural and chemical evolution during dedolomitization: a case study of the Benassal Formation, Maestrat Basin, Spain

Stephen Centrella (1), Nicolas E. Beaudoin (1), Cynthia Trebucq (1), Guilhem Hoareau (1), Enrique Gomez-Rivas (2), Juan Diego Martin-Martin (2), Jean-Paul Callot (1).

1 Universite de Pau et des Pays de l'Adour, E2S UPPA, LFCR, CNRS, TotalEnergies, Pau, France

2 Departament de Mineralogia, Petrologia i Geologia Aplicada, Universitat de Barcelona, Martí i Franquès s/n, 08028 Barcelona, Spain

Correspondence to: Stephen Centrella (centrella.stephen@univ-pau.fr)

This is a post-print version of this article. For the final, copy-edited version please visit:

Centrella, S., Beaudoin, N.E., Trebucq, C. Hoareau, G., Gomez Rivas, E., Martín-Martín, J.D., and Callot, J.-P. 2023. Textural and chemical evolution during dedolomitization: a case study of the Benassal Formation, Maestrat Basin, Spain. Marine and Petroleum Geology, 153, 106290.

https://www.sciencedirect.com/science/article/pii/S0264817223001964

https://doi.org/10.1016/j.marpetgeo.2023.106290

Highlights

- We quantified the element mass transfer during the dedolomitization reaction.
- We refine the reactive fluid pathway and the pH-Eh reaction conditions.
- We determined that the dedolomitization reaction is governed by dissolution-precipitation.

Abstract

The process of dedolomitization (dolomite calcitization) has been the subject of several studies, but the mechanisms that control it are still not fully understood. Dedolomitization, i.e. the replacement of dolomite by calcite, is an important diagenetic process that affects dolostones, in certain cases decreasing the local porosity and altering the rock mechanical properties, reservoir quality and fluid flow pathways. In this contribution we report the petrographic and geochemical evidence of the progressive dedolomitization and its impact on the Lower Cretaceous dolostones of the Benicàssim area (Maestrat Basin, Spain) that host Mississippi Valley Type (MVT) ore deposits. Textural observations and geochemical data suggest that replacement was induced by the interface coupled dissolution-precipitation mechanism. Moreover, quantitative chemical content measurements with mass-balance calculations show that dedolomitization caused a ~ 5% gain of mass during the reaction, associated with 5 vol.% of solid volume increase. The lack of microfracture development suggests that the compensation of such volume increase is achieved by microporosity being filled during calcite precipitation. Considering the meteoric origin of the dedolomitizing fluids, the mass-balance calculation allows estimating the element mass transfer during the reaction. The fact that the fluid was enriched in Zn supports that the fluid was acidic, and likely percolated through the local MVT deposits. Calculation of the required volume of the reactive fluid (10^2 to 10^4 m^3/m^3 dolostone) also shows that thermodynamic calculations overestimates the volume of fluid. This study shows the importance of quantifying mass transfer in diagenetic conditions to better understand metasomatic processes and constrain the fluid pathway in the basin history. As a societal impact, this diagenetic process releases ~ 11 % of the carbon mass but seems to preserve all rare earth elements.

1. Introduction

Among fluid-assisted metasomatic reactions, the mechanism of dolomite calcitization (*i.e.*, dedolomitization) is a very common process that can convert a dolostone into a limestone. Most dedolomites form at, or near to, the Earth's surface where meteoric water infiltrates and gets enriched in calcium by dissolving carbonates (see the complete review of Schoenherr et al., (2018)). In some cases, dedolomitization can happen in burial conditions (Budai et al., 1984). Experimental studies concluded that dedolomitization can operate from less than 50 °C (Groot, 1967) up to 100-200 °C (Stoessell et al., 1987). Dedolomite forms by either (1) "replacement" as interface coupled dissolution-precipitation (James et al., 1993; Kenny, 1992; Putnis and Putnis, 2007) or by (2) the dissolution then precipitation replacement mechanism. The "replacement" mechanism results from the dissolution of the parent mineral coupled to the coeval precipitation of the product mineral within a thin fluidic film defining the reaction interface. The propagation of the reaction interface through the parent mineral depends on the porosity gradient generated in the product mineral, enabling mass transfer from an external fluid reservoir (Putnis, 2009; Putnis and Putnis, 2007; Ruiz-Agudo et al., 2014). Different examples of dedolomitization support the dissolution-precipitation mechanism (Al-Hashimi and Hemingway, 1973; Bischoff et al., 1994; Evamy, 1963; Folkman, 1969; Frank, 1981; Goldberg, 1967; Katz, 1971; Morlot, 1847; Shearman et al., 1961; Vandeginste and John, 2012). The dissolution-precipitation replacement mechanism is a two-step process with first dissolution of dolomite by meteoric groundwater followed by precipitation of calcite infilling newly-formed pores (Kenny, 1992) or from a different solution (James et al., 1993; Jones et al., 1989). A third model explains dedolomitization not as a replacement process but as a new phase related to burial dolomitization (Merino and Canals, 2018). In their pressure-solution self-acceleration model of dolomitization (Merino and Canals, 2011) account for dolomite pseudomorphic properties (i.e. shape and volume conservation during the replacement) by a self-accelerating model starting with the pressure-solution of calcite by newly formed dolomite, releasing Mg^{2+} and Ca^{2+} in the fluid, then producing more dolomite. In that model, dedolomitization is a direct by-product of the process, as once all the Mg^{2+} is consumed by creating dolomite, the Ca^{2+} in the solution starts to precipitate calcite in vacant space in the dolomite.

During a fluid-mediated rock transformation diagenetic fluids can cause strong changes regarding thermal, chemical and mineralogical evolution of the host rock, resulting in important mass transfer (Bebout and Penniston-Dorland, 2016; Centrella et al., 2016, 2015; Manning, 2018, 1994; Putnis and Austrheim, 2013). The rock mechanical and petrophysical properties are modified due to the formation of new mineral assemblages through the incorporation of new chemical components (Putnis, 2009). The impact of the reactive fluid can be documented by chemical and isotopic data from hand samples (Beinlich et al., 2010), but also across replacement interfaces between rocks (Miller et al., 2009), veins (John et al., 2012) and up to kilometre scales (Ague, 2003, 1994; Konrad-Schmolke et al., 2011; Yoshida et al., 2018). In diagenetic conditions, mineral replacement impacts element cycling by for example capturing CO_2 (Ague and Nicolescu, 2014; Whitaker et al., 2004). It also affects reservoir quality of hydrocarbon and carbon storage capacity by closing pores and altering the overall chemical reactivity of the rock (Kirschner and Barnes, 2009; Thibeau et al., 2013). Metasomatism requires the transport of reactive fluid, especially in low-temperature domains, such as the diagenetic one from the near surface to the shallow subsurface. At the basin scale fluid infiltration is facilitated by major faults (Martín-Martín et al., 2015; Salardon et al., 2017) and by diffuse fracture networks (Beaudoin et al., 2014; Evans and Fischer, 2012) and local stylolites (Gomez-Rivas et al., 2022). At the grain scale, reactive fluid percolates between grains depending on the permeability, pore throat size, and pressure of the environment (Centrella et al., 2020; Jonas et al., 2015; Weber et al., 2021). When porosity is low or absent, fluid infiltration can be achieved by the interface coupled dissolution-precipitation mechanism (Centrella et al., 2020; Putnis, 2009) or by growth-driven pressure-solution (Merino and Canals, 2011).

The origin of the fluids responsible of metasomatic reactions, especially in the diagenetic environment, has been the subject of many studies over the last decades (Ferket et al., 2011; Motte et al., 2021; Roure et al., 2010; Salardon et al., 2017; Shah et al., 2012). These studies investigated the origin and/or evolution on the newly formed minerals by measuring trace element content, isotopic ratios, fluid inclusion trapping conditions and compositions. They all aim to estimate the fluid chemical compositions, their temperature and potential interactions with the surrounding host rocks.

Similarly to hydration reactions present in higher *P-T* conditions, the molar volume increases during the transformation of dolomite to calcite (Graf, 1961; Steinfink and Sans, 1959). During this reaction, stress is generated allowing, for example, failure, such as in serpentinization reactions. If fractures are absent, then another mechanism is required to compensate this stress increase, such as a change in the solid volume and mass transfer (open system) (Centrella et al., 2018; Centrella et al., 2016, 2015). A recent study from Centrella et al. (2023), demonstrated that it is possible to estimate the partial fluid chemical composition interacting with a rock in equilibrium with the produced mineral (in this case dolomite), along with the solid volume variation during the reaction. This is based on the quantitative measurement of element concentration in the original calcite and the newly formed dolomite coupled to a mass-balance equation (Grant, 2005, 1986; Gresens, 1967), accounting for the density variation between the two minerals. Here we use the same approach for to study the dedolomitization process (dolomite calcitization).

In this paper we investigate an example of dedolomitization affecting the Late Aptian-earliest Albian carbonates of the Benassal Formation (Fm), in the Maestrat Basin (Spain, Fig. 1). The stratigraphy and paragenesis of this formation has been extensively studied throughout the last decade (Gomez-Rivas et al., 2022; Humphrey et al., 2020; Martín-Martín et al., 2013; Martín-Martín et al., 2012; Tomás, 2007; Tomàs et al., 2007; Yao et al., 2020); Martín-Martín et al., 2015; Martín-Martín et al., 2018; Gomez-Rivas et al., 2014). Previous isotopic and fluid inclusion studies concluded that the observed dedolomitization was related to meteoric fluid circulation linked to the general uplift experienced by the basin between Eocene and Oligocene times (Gomez-Rivas et al., 2012; Roca and Guimerà, 1992; Simón, 2004). Isotopic measurement of $\delta^{18}O$ and $\delta^{13}C$ on the late-stage calcite shows a negative $\delta^{13}C$ trend (up to -9 ‰ PDB), typical of sub-aerial bacterial alteration of the carbon. This trend was interpreted by Martín-Martín et al. (2015) as related to the meteoric origin for the dedolomitizing fluids, that would have more or less interacted with soil as it migrated downward. The present study aims to constrain dedolomitization of the Benassal Fm. dolostones by quantifying the element mass transfer during the reaction between the host dolostone, fluid and the newly formed rock. Using the mass-balance approach of Centrella et al. (2023) on the measured elementary content on each side of a reaction interface, one can calculate the amount of mass gain and mass loss between the fluid and the solid. Considering the origin of the fluid is known, that approach can be used (1) to predict the volume of fluid require to produce the observed calcite, (2) to trace the reactive fluid migration pathway, and (3) to test to distinguish if the studied calcite was formed by direct precipitation (Merino and Canals, 2018) or by a replacement in one step (Putnis, 2009) or two steps (James et al., 1993).

2. Geological setting

2.1 Maestrat Basin

The Maestrat Basin developed in relation to the Late Jurassic to Early Cretaceous rifting of the Iberian Rift System (Salas et al., 2001; Salas and Casas, 1993), and was inverted during the Alpine Orogeny.Mesozoic syn-rift and early Cenozoic contractive structures were reactivated by an extensional phase during the Neogene (Gomez-Rivas et al., 2012; Roca and Guimerà, 1992; Simón, 2004). The study area is located in the SE of the Maestrat Basin, where the intersection between the Benicàssim and the Campello faults formed a semi-graben filled with Upper Jurassic to Lower Cretaceous syn-rift deposits (Martín-Martín et al., 2013) (Fig. 1).

The study area is named the Benicàssim area and is located in the southern part of the Maestrat Basin, in the Penyagolosa sub-basin. It constitutes the eastern margin of the Desert de les Palmes Ranges. The main structures comprise NE-SW to NNE-SSW trending basement faults that enabled Triassic-Lower Cretaceous rocks to crop out (Martín-Martín et al., 2005; Roca et al., 1994). The area is mainly structured by the Benicàssim Fault (NNE-SSW trend and SE dip) and the roughly orthogonal Campello and Juvellús faults (E-W striking and S-dipping) (Gomez-Rivas et al., 2012). The first two faults developed during the Late Jurassic to Early Cretaceous rifting cycle, as evidenced by a very thick Lower Cretaceous sedimentary succession and, accordingly, a significant part of offset of these faults (over a km) likely happened during that rift period, resulting in differences in syn-rift sediment thickness across fault blocks (Yao et al., 2020). Contrarily, the Campello fault offset (around 1 km of stratigraphic offset) was probably associated with the Neogene extension. During the Alpine deformation, all Early Cretaceous

faults were reactivated (Gomez-Rivas et al., 2012). The final regional event is related to the Neogene extension period towards the North (Tomàs et al., 2007). The Lower Cretaceous succession of the Benicàssim area is formed by a stratigraphic sequence comprising: the Barremian Artoles, the Aptian Cervera, Xert, Forcall, Villarroya de los Pinares, and Aptian-Albian Benassal Formations (Salas et al., 2001). Our samples were collected in the Benassal Fm. that host most of the dolostone geobodies (Fig. 1, Gomez-Rivas et al., 2014). The geometry of the dolostones range from massive patches close to the large-scale faults to stratabound geobodies that extend for several kilometres from the faults (Yao et al., 2020). Dolostones close to the Campello fault host Pb-Zn-Ba-Fe-S Mississippi Valley-type (MVT) ore deposits (Martín-Martín et al., 2013).

2.2 The Benassal Formation

The Benassal Formation consists of shallow-marine carbonates with facies rich in rudists, corals and/or orbitolinids (Canérot et al., 1982). This Late Aptian-Early Albian formation lies conformably on an alternation of limestone and marl Aptian formations (Fig. 2a and b) (Martín-Martín et al., 2013). The ramp-type carbonate platform of the Benassal Fm is characterized by three transgressive-regressive sequences (Yao et al., 2020). The top of the Benassal Fm is karstified and overlaid by the clays and sands of the Albian Escucha Formation (Martín-Martín et al., 2013). Dolomitization affects mainly the Benassal Fm of the Benicàssim area composed of more than 1,600 m of carbonate formed in marine shallow-water (Martín-Martín et al., 2013). Gomez-Rivas et al. (2014) estimated that the total volume of dolomitized rock in the 60 km^2 of the Benicàssim area is on the order of 4.10^9 m^3. Unfortunately, no available data are present regarding the volume of dedolomitized rock.

2.3 Paragenetic sequence

The paragenetic sequence affecting the Benassal Fm was reported by Martín-Martín et al. (2015).. These authors described an early calcite cement that precipitated shortly after deposition in a marine environment within inter and intraparticle porosity of the host limestone. The intermediate burial was characterized by the stylolization of the Benassal Fm and the subsequent replacement of limestones by dolostones. The formation of stylolites was followed by the precipitation of dolomite cement (DC) in the primary interparticle and intraparticle porosity of more permeable limestones. The first replacive dolomite (RD1) presents a cloudy aspect due to inclusions and crystals shapes ranging between planar-s to and-planar-a. RD1 is mostly made of dolomite crystals ranging in size from 50 to 600 µm in average, but can reach up to 3 mm. RD1 replaces matrix, grains and early calcite cements. A second replacive dolomite (RD2) is characterized by larger crystal size than RD1 (100 µm to 1.6 mm) and planar-s to non-planar-a texture. RD2 generally formed around RD1 cores forming clear outer rims, which suggests a progressive textural evolution from RD1 to RD2. Dolomite cement (DC) appears as syntaxial overgrowths on RD2 crystals and formed planar-e mosaics with crystal size ranging from 100 to 1500 µm. Saddle dolomite SD1 form large crystals (400 to 5000 µm) with a typical curved shape and undulose extinction. Following the replacement stage, calcite cement CC3 filled vuggy and intercrystalline porosity in dolostones and was followed by the formation of the Pb-Zn MVT ore deposits. The last stage of alteration took place during the uplift and is characterized by the precipitation of calcite cements and the calcitization of dolomite (CC5) phases likely from meteoric waters. Dedolomitization is associated with the formation of thin coating of Fe-oxide within replacive and cement dolomites.

3. Methods

3.1 Sample description and preparation

22 samples including the host limestones, dolostones and dedolomites were collected across the Benassal Fm (Fig. 1b). At the outcrop scale, most of the contacts between the original dolostone and the dedolomite rock display a transition zone affected by stylolites (Fig. 2c, d and e). The petrography of 19 polished thin sections (60 × 45 mm) were analysed by optical microscopy (Nikon Eclipse LV100ND) at the Laboratory of Complex Fluids and their Reservoirs (LFCR, University of Pau and Pays de l'Adour, France).

3.2 Electron probe micro-analyser (EPMA)

Major element compositions of calcite and dolomite were obtained using a Cameca SXFive (Centre de Micro-Caractérisation Raimond Castaing, Toulouse). Analytical conditions were a 10 nA beam current and a 15 keV accelerative voltage, with a beam size of 10 µm, to ensure stability of the material during the analysis. Calibration was performed with natural and synthetic standards: aluminium oxide (Al), magnesium oxide (Mg), wollastonite (Si, Ca), sanidine (K), manganese titanite (Mn), hematite (Fe), albite (Na), barite (Ba), celestine (Sr).

3.3 Electron backscatter diffraction (EBSD)

EBSD analysis was carried out with a SEM JEOL JSM-7100TTLS LV (Centre de Micro-Caractérisation Raimond Castaing, Toulouse). EBSD data were acquired using an Oxford Instruments Aztec 3.4 EBSD and EDS system using an accelerating voltage of 20 keV and a beam size of 1.5 µm and 2 µm. Post-processing of EBSD data was done using the HKL Oxford Instruments Channel 5 v.5.12.72.0 software. Noise reduction was performed by replacing pixels that are different from 8-7 and 6 nearest neighbours (by some misorientation). The EBSD method aims to get crystallographic information from the original dolomite crystals and the newly formed calcite.

3.4 Laser ablation

Polished blocks of around 8x8x4 mm of dolostone and dedolomitized limestone were prepared to measure the trace element content. Samples were measured with a femtosecond laser ablation system (Lambda3; Nexeya, Bordeaux, France) coupled to a high resolution ICP-MS Element XR fitted with the Jet Interface (fsLA/HR-ICP-MS) (Thermo Fisher Scientific instrument, University of Pau & Pays de l'Adour, France). Measurements were performed under dry plasma conditions. The additional Ar carrier gas flow rate, torch position and power were adjusted so that the U/Th ratio was close to 1 +/- 0.05 when ablating the glass SRM NIST612. The reference materials NIST612 and NIST610 were respectively used as primary and secondary calibration standards. ^{43}Ca concentration (wt.%) was used as internal standards for calcite quantification, and ^{25}Mg concentration (wt.%) was used as the internal standard for dolomite quantification (Jochum et al., 2011). ^{25}Mg, ^{43}Ca, ^{57}Fe, ^{55}Mn, ^{51}V, ^{66}Zn, ^{85}Rb, ^{88}Sr, ^{89}Y, ^{139}La, ^{140}Ce, ^{141}Pr, ^{146}Nd, ^{150}Sm, ^{153}Eu, ^{158}Gd, ^{159}Tb, ^{163}Dy, ^{165}Ho, ^{166}Er, ^{169}Tm, ^{172}Yb, ^{175}Lu, ^{208}Pb and ^{238}U were selected in low resolution mode with a dwell time of 30 ms. Images were built from the signal resulting from the sample ablation according to series of horizontal lines, with a scan speed of 1 mm.s^{-1} and a sample translation set to 17 µm.s^{-1} giving a pixels of 17 x 17 µm. Helium stream was fixed to 500 mL.min^{-1}. Once every phase properly quantified, average composition of minerals of the Benassal Formation were extracted from trace elements maps using XMapTools 3.4 (Lanari et al., 2019; Lanari et al., 2014).

Image segmentation was performed by a clustering approach based on pixel densities using the Binary module of XMapTools 4 (Lanari et al., 2019; Lanari et al., 2014). This method consists of defining groups of pixels (i.e. masks) for each phase by delimiting area-of-interest using chemical differences. Oxides could not be properly segmented due to their small size (< 15 µm) but they are mainly associated with calcite

3.5 Mass-balance calculation

The investigation of element mobility during a fluid-mediated reaction requires knowledge of the density, the chemical composition, and the solid volume variation. The overall element gain and loss during the replacement of the dolomite by calcite was estimated using the Gresens mass-balance equation (Gresens, 1967). The mass-balance equation assumes that only one fluid is responsible for the reaction (Eq. 1):

$$f_{\mathrm{v}} \times \left(\frac{d_{\mathrm{Calcite}}}{d_{\mathrm{Dolomite}}}\right) \times C_{\mathrm{Calcite}}^{\mathrm{Element}} - C_{\mathrm{Dolomite}}^{\mathrm{Element}} = x_{\mathrm{Element}} \qquad (1)$$

with f_{v} the volume factor corresponding to the solid volume variation during the reaction, d_i the phase density (g.cm^{-3}) C_i the element concentration measured in a given mineral (in our case in element weight %) and x_i the mass change (in grams). Positive values correspond to a gain of mass (i.e. elements were

brought by the fluid phase) and negative values to a loss of mass (i.e. elements were released to the fluid phase). For a value of $f_v = 1$, no solid volume change is involved between the reactants and the products. Values of $f_v > 1$ and $f_v < 1$ correspond to volume increase or decrease of the solid phase, respectively.

The respective chemical composition of dolomite and calcite correspond to the average values obtained from EPMA (major element) and from fsLA-ICP-MS (trace element). Consequently, the representative stoichiometry of the sample is accounted for (Table 1 and 2). The respective densities of dolomite and calcite were determined as a weighted average of the mineralogical end-members of the solid solution considered. The proportion of each end-member is derived from the measured concentration in the defining element. This approach estimates densities with less than 1% difference from thermodynamically computed density (Centrella et al., 2018). Using a calcite-siderite-magnesite-rhodochrosite system for the calcite solid solution and a dolomite-ankerite-kutnohorite system for the dolomite solid solution, the average densities are 2.72 and 2.85 $g.cm^{-3}$, respectively (Table 1). The following equations (2 & 3) describe such calculations using the average chemical composition of dolomite and calcite:

(Eq. 2): $Density_{dolomite} = (XDol \times DDol) + (XAnk \times DAnk) + (XKut \times DKut)$

With XDol, XAnk and XKut, proportion of dolomite, ankerite and kutnohorite end-member and DDol, DAnk and DKut, respective dolomite, ankerite and kutnohorite density.

(Eq. 3): $Density_{calcite} = (XCal \times DCal) + (XMag \times DMag) + (XSid \times DSid) + (XRho \times DRho)$

With XCal, XMag, XSid and XRho, proportion of calcite, magnesite, siderite and rhodochrosite end-member and XCal, XMag, XSid and XRho, respective calcite, magnesite, siderite and rhodochrosite density.

The solid volume variation during the reaction going from dolomite to calcite can be estimated by assuming one immobile element, by minimizing the flux of mass transfer (Hermann et al., 2013), or by using a textural argument like the abundance of porosity present.

4. Results

4.1 Petrography

The dolostone specimens are characterized by small-size (100 µm to 1 mm) non-pervasive euhedral crystals of replacive dolomite with a cloudy appearance due to a high proportion of solid inclusions. Larger dolomite crystals (1-2 mm equivalent diameter) result from the replacement of echinoderm plate pseudomorphs. Dolomite crystals present an important intracrystalline porosity, around 5 vol.% (RD1 and 2, Fig. 3). For the specific case of porosity, the modal abundance was estimated based on a 2D analyses of BSE images on the dolostone sample using grey value thresholding applied on 8-bits images. In the dedolomitized rock, the replacement of dolomite by calcite forms euhedral to subhedral crystals up to 100 µm in size. In partially replaced dolomites, this calcite fills the intercrystalline porosity of dolomite (Fig. 3e) and selectively replaces the inner rim of the dolomite crystals. The dolomite-calcite interface is rough, exhibiting patterns similar to micro-scale dendrite. This calcite phase corresponds to the meteoric calcites associated with uplift (CC5) described by (Martín-Martín et al., 2015).

4.2 Mineral chemistry

The major element content for both dolomite and calcite is constant throughout the different samples and close to the calcite and dolomite end-member (Table 1). The Fe content ranges between 0.86 and 1.3 wt.% (XAnk. = 0.03) in dolomite, of which the Mn content is close to null (< 0.05 wt.%). The Mg content of calcite ranges around 0.38 wt.% (XMag. = 0.02), while the Fe and Mn content are negligible in the same phase (less than 0.05 wt.%). Both dolomite and calcite chemical composition for major elements is constant even in the vicinity of the replacement interface.

Quantitative trace element concentration maps were collected in the partially dedolomitized sample to visualize the redistribution of trace elements between dolomite and calcite (Fig. 4). Previous data obtained for the dolostone bulk composition from Centrella et al. (2023) were used as reference rock and reported in Table 1. The two elemental maps made in a partially dedolomitized sample (BEN 4, close to the Campello Mine, Fig. 1) show the same results but only one is presented here (Fig. 4). The average trace element concentration for each mineralogical phase for the two partially dedolomitized samples is derived from average phase composition present within maps (Table 2).

The spider diagram (REE) of the studied samples (Fig. 5) represents calcite and dolomite REE content normalized to the world shale element (Piper, 1974). The calcite part measured in the dedolomitized rock exhibits a REE chemical pattern similar to the one of the original dolostone (this study) and of the original limestone (Centrella et al., 2023), by a slightly lower concentration in heavy-REE. The redistribution of the trace elements is relatively homogeneous within the calcite phase but for clarity, only a few elements are presented (Fig. 4).

4.3 Electron backscatter diffraction (EBSD)

Crystallographic orientation of dolomite and calcite were collected with EBSD in the same sample but at a different location than the one trace elements maps have been made. Fig. 6a represents the data of a partially dedolomitized sample (BEN 4A) where the original dolomite (teal) and product calcite (yellow) coexist. The orientation of {10-10},{11-20} and {0001} crystallographic axis is measured at each pixel, and plotted on an equal-area stereonet (lower hemisphere) with respect to the mineralogy. All crystals of dolomite and calcite share an identical crystallographic orientation. The same result arises at the dolomite-calcite interfaces of the sample BEN 4B (Fig. 6b, zone 1 and 2).

5. Interpretation of chemical change using the mass-balance approach

Following the method described above, to be able to quantify the mass transfer between dolomite to calcite, knowledge of the density, the chemical composition, and the solid volume variation is required. Chemical compositions were obtained by analytical measurement, and respective densities were estimated as a weighted average of the mineralogical end-members of the solid solution considered. To estimate the solid volume variation during the reaction we used a textural argument like. In our case, since dolomite (i) contains about 5 vol.% of porosity while calcite have none, and (ii) because no microfractures are visible within both calcite and dolomite (Fig. 3), we assume that the reaction gains 5% of volume, corresponding to the difference in porosity between the parent and the product phases. In terms of mass transfer, assuming: (1) the volume variation of the solid phase (5%), (2) the dolomite and calcite respective densities, and (3) their respective chemical composition, the dedolomitization reaction can be written as follows (Table 2, column “Mass change”):

100 g of dolomite + 0.02 g Mn + 18.46 g Ca + trace elements = 104.58 g calcite + 1.05 g Fe + 11.37 g Mg + 1.48 g C + trace elements (1)

In this model, ~ 105 g of calcite is made from 100 g of dolomite. It results in ~ 5 wt.% of net mass gain brought by the fluid phase. The results of this equation are plotted in percentage of mass change obtained with the Gresens analysis on the isocon diagram in Fig. 7 (Grant, 2005, 1986). All REEs (in light blue) are located within the -20/+20 % of mass change. Due to their initial low concentration in dolomite (below the µg/g or ppm), the mass change below 20 % can be considered as negligeable. Other trace elements that have seen a significant mass variation during the reaction are the Zn and Mn that were brought by the fluids (gain > 100%) and the U, Mg and Fe that were taken away by the fluid.

6. Discussion

6.1 Nature of the fluid composition and the governing process

Isotopic measurements of $\delta^{18}O$ and $\delta^{13}C$ on the late-stage calcite show a negative $\delta^{13}C$ trend (up to -9 ‰ PDB), typical of sub-aerial bacterial alteration of the carbon. This trend was interpreted by Martín-Martín et al. (2015) as related to the meteoric origin for the dedolomitizing fluids, that would have more or less interacted with soil as it migrated downward. However, meteoric water does not usually contain heavy metals (Beverland et al., 1998; Crosbie et al., 2012; Forti et al., 2000; Huang et al., 2008; Romanova et al., 2021), a fact that is inconsistent with our results that the dedolomitizing fluid supplied Zn and Rb to the mineralogical system (Fig. 7). As an example, almost all the Zn concentration from rainfall in Australia reported by Crosbie et al. (2012) are below 0.2 mg/L. In our case study, 100 g of dolomite reacts with 3.65 mg of Zn carried in the fluid (Table 1, column "Mass change"). Then, assuming that the fluid origin is meteoric, on the basis of isotopic data, the fluid chemical composition at the time of the reaction requires an interaction between the meteoric water and a Zn-Rb source. The MVT deposits in the Benassal Formation contain the following minerals: galena (Pb-rich), sphalerite (Zn-rich), barite (Ba and S-rich), goethite and hematite (Fe-rich) and pyrite (S-rich) Martín-Martín et al. (2013). To explain the enrichment in Zn of the fluid but not Pb or Fe, interaction with the MVT deposits, an acidic fluid (pH < 7) can be invoked as the relative mobility of the Zn^{2+} is much higher than Pb^{2+} at low pH (Förstner, 1985). Additionally, the redox conditions of dedolomitization can be obtained using trace elements such as Mn, V and U (Chen et al., 2015; Huang et al., 2011; Zhang et al., 2014). Except for Mn, V and U that are lost during the reaction, which could indicate a general oxidizing environment (Zhang et al., 2014). The net (i) enrichment in heavy metals like Zn and Pb and (ii) loss in redox-sensitive element like Fe, U and V, allow us to propose that the dedolomitizing fluid was acidic, and migrated from the surface to the Benassal Formation through the MVT deposit under a general oxidizing environment.

6.2 Amount of fluid required to replace dolostones

The mass-balance approach allows calculation of the volume of fluid required to complete the dedolomitization of the observed dolomite rock volume (Centrella et al., 2023). As expected, the mass of Ca required to replace dolomite by calcite is by far larger than the mass of any other elements (Eq. 1). In order to estimate the volume of fluid involved in the dedolomitization process, we use the result of the mass-balance equation (Eq. 1) with Ca as a reference element. We estimate the amount of fluid required to replace 100 g of original dolomite considering a fixed Ca concentration in the input fluid. Because we do not have the initial meteoric water chemical composition, we assumed it had a Ca concentration equivalent of that of present-day meteoric water. That returns a wide range of Ca concentration, from 60 to 5900 mg/L (Beverland et al., 1998; Crosbie et al., 2012; Forti et al., 2000; Huang et al., 2008; Romanova et al., 2021). Using the mass-balance model, 18.46 g of Ca is required to dedolomitize 100 g of dolomite (Eq. 1). Considering a water with a Ca concentration of 60 mg/L, this mass corresponds to 307 L, equivalent to 8767 m^3 of water per m^3 of dolomite. Considering the highest value, the volume of water decreases to 3 L/100 g of dolomite, equivalent to almost 90 m^3 by m^3 of dolostone. Other studies based on reactive transport modelling reported large volumes of fluid required to cause dedolomitization (Escorcia et al., 2013). The magnitude of fluid flux through rocks undergoing metasomatism is still under debate with arguments for large volume of fluid (Ague, 1991; Centrella, 2019; Centrella et al., 2016, 2015; Ferry, 1994; Gomez-Rivas et al., 2014) or against them (Yardley et al., 2014). The first argument supporting large volumes of fluid is based on the calculation of the amount of fluid required to remove or add material during the metasomatic processes. The counter argument, especially for retrograde metamorphism, argues that very little free fluid can exist because hydration reaction rates are fast relative to fluid infiltration (Yardley et al., 2014). Escorcia et al. (2013) simulated the fluid responsible of dedolomitization of the Benassal Fm using two different geochemical simulation approaches: (i) considering equilibrium between the selected fluid and the reacting dolostone, and (ii) considering kinetic rate laws for dissolution and precipitation of minerals with reactive transport modelling. They proposed that dedolomitization is a slow process triggered by meteoric water warmed up to < 50 °C. Coupled with thermodynamic data, they estimated that to replace a m^3 of dolostone, 10^5-

10^6 m^3 of meteoric, or groundwater fluid is required. These results are between one to three orders of magnitude above the volumes we predict.

Results from the mass balance approach show that a net + 5 % of mass is associated with the replacement of dolomite by calcite (Eq. 1). Converting this per cubic meter of rock mean that when the fluid interacts with the solid dolostone, 100 kg of mass is lost through the fluid phase. It is difficult to properly constrain its impact on basin subsidence but it might be negligible (Martín-Martín et al., 2013).

6.3 Replacement process

Our study brings some data that can help answer the question as to what is the main process driving the replacement or if there was a replacement at all. First and foremost, textural and crystallographic observations support the interpretation that this was a replacement process rather than precipitation alone: (i) the reaction with calcite grains seemingly involves dolomite dissolution, as witnessed by identified micro-scale dendrite-like patterns (Fig. 3e and 6), symptomatic of dissolution in granular media (Eriksen et al., 2015; Golfier et al., 2002; Xu et al., 2018) and (ii) the preservation of crystallographic information of the parent dolomite in the calcite (Fig. 6), is a strong support of the interface-coupled dissolution precipitation. Furthermore, the replacement texture is crystallographically controlled, as attested by the preserved rhombohedral shape of dolomite crystals (Fig. 3a-d).

Second, the mass transfer of REE is insightful. REE are highly insoluble, poorly mobile, and incompatible elements. As a consequence, their patterns as seen on a spider diagram often remain unchanged during metamorphism/metasomatism (White, 2013). For example, the negative anomaly in Ce and Tb and the positive anomaly in Sm seen in the dedolomite are also visible in the dolostone. Yet, REE comprises highly incompatible elements (light rare earth elements-LREE) and less incompatible (heavy rare earth elements-HREE) in a way that suggests a more efficient partitioning of the LREE in the fluid that in the mineral during metasomatism. This suggests that the newly formed calcite will tend to incorporate more light-REE than heavy-REE and this is what we see in Table 2 and Figure 7. The results obtained from the mass-balance calculation presented in Figure 7 show that all REEs are close to the no gain/no loss line, that may reflect the kinetics of the replacement reaction relative to the element mobility. If the REE composition does not change significantly between parent and product phase (Fig. 5), the dissolution–precipitation process governing the dedolomitization has to be sufficiently fast to retain the supposed more mobile elements (Centrella et al., 2016). That would be in favour of an interface-coupled dissolution-precipitation process. Similar textural observations have been described in analogous reactions of serpentinization. Plümper et al. (2012) showed that the lack of porosity in product serpentine and the absence of stress markers such as edge pits in olivine confirm a reaction in which the dissolution rate equals the precipitation rate. A similar observation and conclusion can be made for the replacement of dolomite by calcite. The relative solubility of the dolomite and product calcite in the fluid will determine how much material is dissolved relative to the amount reprecipitated.

As described by Martín-Martín et al. (2013) and Yao et al. (2020), dolostone geobodies are stratabound and distributed in the vicinity of major faults implying a control of the host rocks and faults during the interaction with hydrothermal Mg-rich fluids (Gomez-Rivas et al., 2014). The same fault network was likely used by the meteoric fluid responsible for the dedolomitization of the Benassal Fm (Martín-Martín et al., 2013). From the analyses of our samples, we propose a dedolomitization model at the crystal and rock scale, controlled by element mass transfer and textural analyses (Fig. 8). Percolation of the dedolomitizing fluid through the dolostone allowed by the dissolution-precipitation mechanism at the interface, supported by both similar REE pattern (Fig. 5) and the preservation of crystallographic axes from dolomite to the newly formed calcite (Fig. 6).

The investigation of the dedolomitization process using chemical and textural data push forward our understanding of diagenetic process at low pressure and temperature conditions. Textural similarities between parent and daughter minerals with reactions from higher pressure-temperature conditions confirm similar mechanism governing the fluid-mediated rock transformation. Discussed by the metamorphic community but less by the diagenetic one, this study confirms a close relationship between

(i) open and close system regarding mass transfer, (ii) density change, (iii) solid volume variation and (iv) stress generation due to hydration reaction.

7. Conclusion

The detailed investigation of crystallographic and chemical patterns at the interface between original dolostone and dedolomitized rock allows interpretation of the origin and pathways of the meteoric fluids along with the redox and pH conditions of the replacement in the Benassal Fm. Using a mass-balance approach, we propose that an acidic meteoric fluid percolated through major faults and across MVT deposits in the vicinity of the burial dolostone, before replacing it by calcite in an oxidized environment. This is testified by the fact the calcite crystals are associated with a gain in Zn, Mn, Ca, LREE and Rb, along the crystal structure compared to the precursor dolomite. The patterns associated with the dolomite-calcite contact crystals suggest a propagation of dedolomitization controlled by both the previously described replacement mechanisms. Indeed, dendrite like patterns at the contact support a sequence of dissolution of dolomite followed by precipitation of calcite, while the conservation of the crystallographic axes and the no gain/no loss of the REE during the reaction supports the one-step interface-coupled dissolution-precipitation mechanism. The involvement of the latter mechanism, already well-known under higher pressure and temperature conditions (metamorphism), is seldomly considered in the *P-T* conditions of dedolomitization (< 50 °C).

Beyond the case of the Benassal Fm., the mass-balance calculations show that dedolomitization involves a net mass gain of ca. 5 wt.%, implying a gain of about 100 kg per cubic meter. This process is associated with a gain of solid volume closing the original porosity present in the dolomite crystals. The amount of fluid required to permit the reaction, i.e. between $10^{\wedge 2}$ and $10^{\wedge 4}$ m^3 per m^3 of dolostone, is between 1 to 4 order of magnitude below previous studies based on reactive transport simulation and thermodynamic, highlighting the complexity of fluid-mediated replacement of rocks in nature.

By quantifying mass transfer associated to dedolomitization reaction, it allowed us to constrain the fluid pathways in the basin history, its redox conditions, its pH and the governing mechanism of the reaction, i.e. interface coupled dissolution-precipitation mechanism. This reaction occurs near the surface and releases 11 % of the carbon mass from the original dolostone but tends to preserve Rare Earth Elements.

Acknowledgements

This work is funded by the project TXM-R2 (Institut Carnot ISiFOR), S.C. and N.B. are funded through the isite-E2S, supported by the ANR PIA and the Région Nouvelle-Aquitaine. We thank Arnaud Proietti for the EBSD analyses and the help for the data processing, Christophe Pécheyran and Fanny Claverie for the fs-LA-ICP-MS analyses and the help for the data processing. EGR acknowledges funding by the Spanish Ministry of Science and Innovation / State Research Agency of Spain (AEI) / European Regional Development Fund (ERDF) /10.13039/501100011033 ("Ramón y Cajal" fellowship RYC2018-026335-I and research project PID2020-118999GB-I00). JDM acknowledges funding by the Spanish DGICYT research project PID2021-122467NB-C22. We would like to thank two anonymous reviewers for their critical and valuable reviews.

References

Ague, J.J., 1991. Evidence for major mass transfer and volume strain during regional metamorphism of pelites. Geology 19, 855–858.

Ague, J.J., 1994. Mass transfer during Barrovian metamorphism of pelites, South-Central Connecticut. I: Evidence for changes in composition and volume. American Journal of Science 294, 989–1057.

Ague, J.J., 2003. Fluid Infiltration and Transport of Major, Minor, and Trace Elements During Regional Metamorphism of Carbonate Rocks, Wepawaug Schist, Connecticut, USA. American Journal of Science 303, 753–816. https://doi.org/10.2475/ajs.303.9.753.

Ague, J.J., Nicolescu, S., 2014. Carbon dioxide released from subduction zones by fluid-mediated reactions. Nature Geosci 7, 355–360. https://doi.org/10.1038/ngeo2143.
Al-Hashimi, W.S., Hemingway, J.E., 1973. Recent dedolomitization and the origin of the rusty crusts of Northumberland. Journal of Sedimentary Petrology 43, 82–91.
Beaudoin, N., Bellahsen, N., Lacombe, O., Emmanuel, L., Pironon, J., 2014. Crustal-scale fluid flow during the tectonic evolution of the Bighorn Basin (Wyoming, USA). Basin Res 26, 403–435. https://doi.org/10.1111/bre.12032.
Bebout, G.E., Penniston-Dorland, S.C., 2016. Fluid and mass transfer at subduction interfaces—The field metamorphic record. Lithos 240-243, 228–258. https://doi.org/10.1016/j.lithos.2015.10.007.
Beinlich, A., Austrheim, H., Glodny, J., Erambert, M., Andersen, T.B., 2010. CO_2 sequestration and extreme Mg depletion in serpentinized peridotite clasts from the Devonian Solund basin, SW-Norway. Geochimica et Cosmochimica Acta 74, 6935–6964. https://doi.org/10.1016/j.gca.2010.07.027.
Beverland, I., Crowther, J., Srinivas, M., Heal, M., 1998. The influence of meteorology and atmospheric transport patterns on the chemical composition of rainfall in south-east England. Atmospheric Environment 32, 1039–1048. https://doi.org/10.1016/S1352-2310(97)00365-8.
Bischoff, J.L., Juliá, R., Shanks, I.W., Rosenbauer, R.J., 1994. Karstification without carbonic acid: Bedrock dissolution by gypsum-driven dedolomitization. Geol 22, 995. https://doi.org/10.1130/0091-7613(1994)022<0995:KWCABD>2.3.CO;2.
Bover-Arnal, T., Martín-Martín, J.D., Gomez-Rivas, E., Travé, A., Salas, R., Moreno-Bedmar, J.A., Tomás, S., 2009. Insights into the upper aptian carbonate succession the south-eastern maestrat basin (e iberia), in: , pp. 123–128.
Budai, J.M., Lohmann R. K. C., Owen, R.M., 1984. Burial Dedolomite in the Mississippian Madison Limestone, Wyoming and Utah Thrust Belt. SEPM JSR Vol. 54. https://doi.org/10.1306/212F83FF-2B24-11D7-8648000102C1865D.
Canérot, J., Cugny, P., Pardo, G., Salas, R., Villena, J., 1982. El Cretácico de España. Universidad Complutense de Madrid.
Centrella, S., 2019. The granulite- to eclogite- and amphibolite-facies transition: a volume and mass transfer study in the Lindås Nappe, Bergen Arcs, west Norway, 241–263. https://doi.org/10.1144/SP478.9.
Centrella, S., Austrheim, H., Putnis, A., 2015. Coupled mass transfer through a fluid phase and volume preservation during the hydration of granulite: An example from the Bergen Arcs, Norway. Lithos 236-237, 245–255. https://doi.org/10.1016/j.lithos.2015.09.010.
Centrella, S., Austrheim, H., Putnis, A., 2016. Mass transfer and trace element redistribution during hydration of granulites in the Bergen Arcs, Norway. Lithos 262, 1–10. https://doi.org/10.1016/j.lithos.2016.06.019.
Centrella, S., Beaudoin, N.E., Derluyn, H., Motte, G., Hoareau, G., Lanari, P., Piccoli, F., Pecheyran, C., Callot, J.-P., 2020. Micro-scale chemical and physical patterns in an interface of hydrothermal dolomitization reveals the governing transport mechanisms in nature: case of the Layens anticline, Pyrenees, France. Sedimentology. https://doi.org/10.1111/sed.12808.
Centrella, S., Hoareau, G., Beaudoin, N.E., Motte, G., Lanari, P., Piccoli, F., Callot, J.-P., Gomez-Rivas, E., Martín-Martín, J.D., 2023. Estimating the fluid composition after dolomitization using mass balance equation: comparison of examples from Spain, Canada and France. Global and Planetary Change 220, 104016. https://doi.org/10.1016/j.gloplacha.2022.104016.
Centrella, S., Putnis, A., Lanari, P., Austrheim, H., 2018. Textural and chemical evolution of pyroxene during hydration and deformation: A consequence of retrograde metamorphism. Lithos 296-299, 245–264. https://doi.org/10.1016/j.lithos.2017.11.002.
Chen, Y., Chu, X.L., Zhang, X.L., Zhai, M.G., 2015. Carbon isotopes, sulfur isotopes, and trace elements of the dolomites from the Dengying Formation in Zhenba area, southern Shaanxi: Implications for shallow water redox conditions during the terminal Ediacaran. Sci. China Earth Sci. 58, 1107–1122. https://doi.org/10.1007/s11430-015-5071-0.

Crosbie, R., Morrow, D., Cresswell, R., Leaney, F., Lamontagne, S., Lefournour, M., 2012. New insights to the chemical and isotopic composition of rainfall across Australia.
Eriksen, F.K., Toussaint, R., Måløy, K.J., Flekkøy, E.G., 2015. Invasion patterns during two-phase flow in deformable porous media. Front. Phys. 3, 312. https://doi.org/10.3389/fphy.2015.00081.
Escorcia, J.-.C., Gomez-Rivas, E., Daniele, L., Corbella, M., 2013. Dedolomitization and reservoir quality: insights from reactive transport modelling. Geofluids. https://doi.org/10.1111/gfl.12023.
Evamy, B.D., 1963. The application of chemical staining technique to a study of dedolomitization. Sedimentology 2, 164–170. https://doi.org/10.1111/j.1365-3091.1963.tb01210.x.
Evans, M.A., Fischer, M.P., 2012. On the distribution of fluids in folds: A review of controlling factors and processes. Journal of Structural Geology 44, 2–24. https://doi.org/10.1016/j.jsg.2012.08.003.
Ferket, H., Guilhaumou, N., Roure, F., Swennen, R., 2011. Insights from fluid inclusions, thermal and PVT modeling for paleo-burial and thermal reconstruction of the Córdoba petroleum system (NE Mexico). Marine and Petroleum Geology 28, 936–958. https://doi.org/10.1016/j.marpetgeo.2010.01.020.
Ferry, J.M., 1994. Overview of the petrologic record of fluid flow during regional metamorphism in northern New Zealand. American Journal of Science 294, 905–988.
Folkman, Y., 1969. Diagenetic dedolomitization in the Albian–Cenomanian Yagur dolomite on Mount Carmel (northern Israel). Journal of Sedimentary Petrology 39, 380–385. https://doi.org/10.1306/74D71C8F-2B21-11D7-8648000102C1865D.
Förstner, U., 1985. Chemical forms and reactivities of metals in sediments.
Forti, M.C., Melfi, A.J., Astolfo, R., Fostier, A.-H., 2000. Rainfall chemistry composition in two ecosystems in the northeastern Brazilian Amazon (Amapá State). J. Geophys. Res. 105, 28895–28905. https://doi.org/10.1029/2000JD900235.
Frank, J.R., 1981. Dedolomitization in the Taum Sauk limestone (Upper Cambrian), Southeast Missouri. Journal of Sedimentary Research 51, 7–18. https://doi.org/10.1306/212F7BF3-2B24-11D7-8648000102C1865D.
Goldberg, M., 1967. Supratidal Dolomitization and Dedolomitization in Jurassic Rocks of Hamakhtesh Haqatan, Israel. Journal of Sedimentary Petrology 37, 760–773.
Golfier, F., Zarcone, C., Bazin, B., Lenormand, R., Lasseux, D., Quintard, M., 2002. On the ability of a Darcy-scale model to capture wormhole formation during the dissolution of a porous medium. J. Fluid Mech. 457, 213–254. https://doi.org/10.1017/S0022112002007735.
Gomez-Rivas, E., Corbella, M., Martín-Martín, J.D., Stafford, S.L., Teixell, A., Bons, P.D., Griera, A., Cardellach, E., 2014. Reactivity of dolomitizing fluids and Mg source evaluation of fault-controlled dolomitization at the Benicàssim outcrop analogue (Maestrat basin, E Spain). Marine and Petroleum Geology 55, 26–42. https://doi.org/10.1016/j.marpetgeo.2013.12.015.
Gomez-Rivas, E., Martín-Martín, J.D., Bons, P., Koehn, D., Griera, A., Travé, A., Llorens, M.-G., Humphrey, E., Neilson, J., 2022. Stylolites and stylolite networks as primary controls on the geometry and distribution of carbonate diagenetic alterations. Marine and Petroleum Geology 136. https://doi.org/10.1016/j.marpetgeo.2021.105444.
Gomez-Rivas, E., Warber, K., Kulzer, F., Bons, P.D., Koehn, D., Martín-Martín, J.D., 2012. Structural evolution of the Benicassim area (Maestrat basin, NE Spain): insights from fracture and vein analysis. Geogaceta 51, 79–82.
Graf, D.L., 1961. Crystallographic tables for the rhombohedral carbonates. American Mineralogist 46, 1283–1316.
Grant, J.A., 1986. The Isocon Diagram-A Simple Solution to Gresens' Equation for Metasomatic Alteration. Economic Geology 81, 1976–1982.
Grant, J.A., 2005. Isocon analysis: A brief review of the method and applications. Physics and Chemistry of the Earth, Parts A/B/C 30, 997–1004. https://doi.org/10.1016/j.pce.2004.11.003.
Gresens, R.L., 1967. Composition-Volume relationships of metasomatism. Chemical Geology 2, 47–65.

Groot, K. de, 1967. Experimental Dedolomitization. Journal of Sedimentary Petrology 37, 1216–1220.
Hermann, J., Zheng, Y.-F., Rubatto, D., 2013. Deep Fluids in Subducted Continental Crust. Elements 9, 281–287. https://doi.org/10.2113/gselements.9.4.281.
Huang, J., Chu, X., Jiang, G., Feng, L., Chang, H., 2011. Hydrothermal origin of elevated iron, manganese and redox-sensitive trace elements in the c . 635 Ma Doushantuo cap carbonate. Journal of the Geological Society 168, 805–816. https://doi.org/10.1144/0016-76492010-132.
Huang, Y., Wang, Y., Zhang, L., 2008. Long-term trend of chemical composition of wet atmospheric precipitation during 1986–2006 at Shenzhen City, China. Atmospheric Environment 42, 3740–3750. https://doi.org/10.1016/j.atmosenv.2007.12.063.
Humphrey, E., Gomez-Rivas, E., Neilson, J., Martín-Martín, J.D., Healy, D., Yao, S., Bons, P.D., 2020. Quantitative analysis of stylolite networks in different platform carbonate facies. Marine and Petroleum Geology 114, 104203. https://doi.org/10.1016/j.marpetgeo.2019.104203.
James, N.P., Bone, Y., Kyser, T.K., 1993. Shallow Burial Dolomitization and Dedolomitization of Mid-Cenozoic, Cool-Water, Calcitic, Deep-Self Limestones, Southern Australia. Journal of Sedimentary Research 63, 528–538.
Jochum, K.P., Weis, U., Stoll, B., Kuzmin, D., Yang, Q., Raczek, I., Jacob, D.E., Stracke, A., Birbaum, K., Frick, D.A., Günther, D., Enzweiler, J., 2011. Determination of Reference Values for NIST SRM 610-617 Glasses Following ISO Guidelines. Geostandards and Geoanalytical Research 35, 397–429. https://doi.org/10.1111/j.1751-908X.2011.00120.x.
John, T., Gussone, N., Podladchikov, Y.Y., Bebout, G.E., Dohmen, R., Halama, R., Klemd, R., Magna, T., Seitz, H.-M., 2012. Volcanic arcs fed by rapid pulsed fluid flow through subducting slabs. Nature Geosci 5, 489–492. https://doi.org/10.1038/ngeo1482.
Jonas, L., Müller, T., Dohmen, R., Baumgartner, L., Putlitz, B., 2015. Transport-controlled hydrothermal replacement of calcite by Mg-carbonates. Geology 43, 779–782. https://doi.org/10.1130/G36934.1.
Jones, B., Pleydell, S.M., Kwoi-Choi, N., Longstaffe, F.J., 1989. Formation of poikilotopic calcite–dolomite fabrics in the Oligocene–Miocene Bluff formation of Grand Cayman, British West Indies:. Bulletin of Canadian Petroleum Geology 37, 255–265.
Katz, A., 1971. Zoned Dolomite Crystals. The Journal of Geology 79, 38–51. https://doi.org/10.1086/627585.
Kenny, R., 1992. Origin of disconformity dedolomite in the martin formation (Late Devonian, Northern Arizona). Sedimentary Geology 78, 137–146. https://doi.org/10.1016/0037-0738(92)90117-A.
Kirschner, J.P., Barnes, D.A., 2009. Geological sequestration capacity of the Dundee Limestone, Michigan Basin, United States. Environ. Geosci. 16, 127–138. https://doi.org/10.1306/eg.04240909007.
Konrad-Schmolke, M., O'Brien, P.J., Zack, T., 2011. Fluid Migration above a Subducted Slab—Constraints on Amount, Pathways and Major Element Mobility from Partially Overprinted Eclogite-facies Rocks (Sesia Zone, Western Alps). Journal of Petrology 52, 457–486. https://doi.org/10.1093/petrology/egq087.
Lanari, P., Vho, A., Bovay, T., Airaghi, L., Centrella, S., 2019. Quantitative compositional mapping of mineral phases by electron probe micro-analyser. Geological Society, London, Special Publications 478, 39–63. https://doi.org/10.1144/SP478.4.
Lanari, P., Vidal, O., Andrade, V.d., Dubacq, B., Lewin, E., Grosch, E.G., Schwartz, S., 2014. XMapTools: A MATLAB©-based program for electron microprobe X-ray image processing and geothermobarometry. Computers & Geosciences 62, 227–240. https://doi.org/10.1016/j.cageo.2013.08.010.
Manning, C.E., 1994. The solubility of quartz in H_2O in the lower crust and upper mantle. Geochimica et Cosmochimica Acta 58, 4831–4839.
Manning, C.E., 2018. Fluids of the Lower Crust: Deep Is Different. Annu. Rev. Earth Planet. Sci. 46, 67–97. https://doi.org/10.1146/annurev-earth-060614-105224.

Martín-Martín, J.D., Gomez-Rivas, E., Bover-Arnal, T., Travé, A., Salas, R., Moreno-Bedmar, J.A., Tomás, S., Corbella, M., Teixell, A., Vergés, J., Stafford, S.L., 2013. The Upper Aptian to Lower Albian syn-rift carbonate succession of the southern Maestrat Basin (Spain): Facies architecture and fault-controlled stratabound dolostones. Cretaceous Research 41, 217–236. https://doi.org/10.1016/j.cretres.2012.12.008.

Martín-Martín, J.D., Gomez-Rivas, E., Travé, A., Salas, R., Vergés, J., 2012. Dolomías controladas por fracturas en carbonatos aptienses de la zona de Benicàssim (SE Cuenca del Maestrat): distribución y características petrogràficas. Geogaceta 51, 19–22.

Martín-Martín, J.D., Sanfelíu, T., Gómez-Gras, D., 2005. Mineralogía de arcillas cerámicas: El Permo-Trías de Castelló. Publicacions de la Universitat.

Martín-Martín, J.D., Travé, A., Gomez-Rivas, E., Salas, R., Sizun, J.-P., Vergés, J., Corbella, M., Stafford, S.L., Alfonso, P., 2015. Fault-controlled and stratabound dolostones in the Late Aptian–earliest Albian Benassal Formation (Maestrat Basin, E Spain): Petrology and geochemistry constrains. Marine and Petroleum Geology 65, 83–102. https://doi.org/10.1016/j.marpetgeo.2015.03.019.

Merino, E., Canals, A., 2011. Self-accelerating dolomite for calcite replacement: self organized synamics of burial dolomitization and associated mineralization. American Journal of Science 311, 573–607. https://doi.org/10.2475/07.2011.01.

Merino, E., Canals, À., 2018. Reply: (Reply to the Comment by David W. Morrow on "Self-accelerating dolomite-for-calcite replacement: Self-organized dynamics of burial dolomitization and associated mineralization", v. 311, n. 7, p. 573–607.). Am J Sci 318, 887–892. https://doi.org/10.2475/08.2818.04.

Miller, D.P., Marschall, H.R., Schumacher, J.C., 2009. Metasomatic formation and petrology of blueschist-facies hybrid rocks from Syros (Greece): Implications for reactions at the slab–mantle interface. Lithos 107, 53–67. https://doi.org/10.1016/j.lithos.2008.07.015.

Morlot, A. von, 1847. Veber Dolomit und seine Kunstliche Darstelling aus Kalkstein. Naturwissenschaftliche Abhandlungen 1, 305–315.

Motte, G., Hoareau, G., Callot, J.-P., Révillon, S., Piccoli, F., Calassou, S., Gaucher, E.C., 2021. Rift and salt-related multi-phased dolomitization: example from the northwestern Pyrenees. Marine and Petroleum Geology 126. https://doi.org/10.1016/j.marpetgeo.2021.104932.

Piper, D.Z., 1974. Rare Earh Elements in the Sedimentary Cycle: A Summary. Chemical Geology 14, 285–304.

Plümper, O., Røyne, A., Magrasó, A., Jamtveit, B., 2012. The interface-scale mechanism of reaction-induced fracturing during serpentinization. Geology 40, 1103–1106. https://doi.org/10.1130/G33390.1.

Putnis, A., 2009. Mineral Replacement Reactions. Reviews in Mineralogy and Geochemistry 70, 87–124. https://doi.org/10.2138/rmg.2009.70.3.

Putnis, A., Austrheim, H., 2013. Mechanisms of Metasomatism and Metamorphism on the Local Mineral Scale: The Role of Dissolution-Reprecipitation During Mineral Re-equilibration, in: Harlov, D.E., Austrheim, H. (Eds.), Metasomatism and the Chemical Transformation of Rock, vol. 294. Springer Berlin Heidelberg, Berlin, Heidelberg, pp. 141–170.

Putnis, A., Putnis, C.V., 2007. The mechanism of reequilibration of solids in the presence of a fluid phase. Journal of Solid State Chemistry 180, 1783–1786. https://doi.org/10.1016/j.jssc.2007.03.023.

Roca, E., Guimerà, J., 1992. The Neogene structure of the eastern Iberian margin: Structural constraints on the crustal evolution of the Valencia trough (western Mediterranean). Tectonophysics 203, 203–218. https://doi.org/10.1016/0040-1951(92)90224-T.

Roca, E., Guimerà, J., Salas, R., 1994. Mesozoic extensional tectonics in the southeast Iberian Chain. Geological Magazine 131, 155–168.

Romanova, A., Porowski, A., Zielski, T., Dancewicz, A., 2021. Origin and evolution of chemical composition of mineral waters of Szczawno-Zdrój inferred from long-term variation of ionic

ratios, Sudetes Mts. (SW Poland). Environ Earth Sci 80. https://doi.org/10.1007/s12665-021-09643-1.

Roure, F., Andriessen, P., Callot, J.P., Faure, J.L., Ferket, H., Gonzales, E., Guilhaumou, N., Lacombe, O., Malandain, J., Sassi, W., Schneider, F., Swennen, R., Vilasi, N., 2010. The use of palaeo-thermo-barometers and coupled thermal, fluid flow and pore-fluid pressure modelling for hydrocarbon and reservoir prediction in fold and thrust belts. Geological Society, London, Special Publications 348, 87–114. https://doi.org/10.1144/SP348.6.

Ruiz-Agudo, E., Putnis, C.V., Putnis, A., 2014. Coupled dissolution and precipitation at mineral–fluid interfaces. Chemical Geology 383, 132–146. https://doi.org/10.1016/j.chemgeo.2014.06.007.

Salardon, R., Carpentier, C., Bellahsen, N., Pironon, J., France-Lanord, C., 2017. Interactions between tectonics and fluid circulations in an inverted hyper-extended basin: Example of mesozoic carbonate rocks of the western North Pyrenean Zone (Chaînons Béarnais, France). Marine and Petroleum Geology 80, 563–586. https://doi.org/10.1016/j.marpetgeo.2016.11.018.

Salas, R., Casas, A., 1993. Mesozoic extensional tectonics, stratigraphy and crustal evolution during the Alpine cycle of the eastern Iberian basin. Tectonophysics 228, 33–55. https://doi.org/10.1016/0040-1951(93)90213-4.

Salas, R., Guimeri, J., Mas, R., Martin-Closas, C., Meléndez, A., Alonso, A., 2001. Evolution of the Mesozoic Central Iberian Rift System and its Cainozoic inversion (Iberian chain). Mém. Mus. natl. hist. nat. (1993) 186, 145–186.

Schoenherr, J., Reuning, L., Hallenberger, M., Lüders, V., Lemmens, L., Biehl, B.C., Lewin, A., Leupold, M., Wimmers, K., Strohmenger, C.J., 2018. Dedolomitization: review and case study of uncommon mesogenetic formation conditions. Earth-Science Reviews 185, 780–805. https://doi.org/10.1016/j.earscirev.2018.07.005.

Shah, M.M., Nader, F.H., Garcia, D., Swennen, R., Ellam, R., 2012. Hydrothermal Dolomites in the Early Albian (Cretaceous) Platform Carbonates (NW Spain): Nature and Origin of Dolomites and Dolomitising Fluids. Oil Gas Sci. Technol. – Rev. IFP Energies nouvelles 67, 97–122. https://doi.org/10.2516/ogst/2011174.

Shearman, D.J., Khouri, J., Taha, S., 1961. On the replacement of dolomite by calcite in some mesozoic limestones from the French Jura. Proceedings of the Geologists' Association 72, 1-12. https://doi.org/10.1016/S0016-7878(61)80021-7.

Simón, J.L., 2004. La estructura extensional neógena-cuaternaria en la Cordillera Ibérica. Geologıa de Espaa. Sociedad Geológica de Espaa-IGME, Madrid, 615–617.

Steinfink, H., Sans, F.J., 1959. Refinement of the crystal structure of dolomite. American Mineralogist 44, 679–682.

Stoessell, R., Klimentidis, R., Prezbindowski, D., 1987. Dedolomitization in Na□Ca□Cl brines from 100° to 200°C at 300 bars. Geochimica et Cosmochimica Acta 51, 847–855. https://doi.org/10.1016/0016-7037(87)90098-6.

Thibeau, S., Chiquet, P., Prinet, C., Lescanne, M., 2013. Lacq-Rousse CO2 Capture and Storage Demonstration Pilot: Lessons Learnt from Reservoir Modelling Studies. Energy Procedia 37, 6306–6316. https://doi.org/10.1016/j.egypro.2013.06.559.

Tomás, S., 2007. Sistemas arrecifales del Cretácico inferior de la Cuenca del Maestrat. Modelos deposicionales, paleontológicos y diagenéticos. Unpublished PhD thesis, Universitat de Barcelona, Spain.

Tomàs, S., Comas Nebot, M., Salas, R., 2007. La plataforma carbonatada Aptiense superior de Benicàssim-Orpesa (Cuenca del Maestrat, Cadena Ibérica): modelo de depósito. Geogaceta 41, 235–238.

Vandeginste, V., John, C.M., 2012. Influence of climate and dolomite composition on dedolomitization: insights from a multi-proxy study in the central Oman Mountains. Journal of Sedimentary Research 82, 177–195. https://doi.org/10.2110/jsr.2012.19.

Weber, J., Cheshire, M.C., Bleuel, M., Mildner, D., Chang, Y.-J., Ievlev, A., Littrell, K.C., Ilavsky, J., Stack, A.G., Anovitz, L.M., 2021. Influence of microstructure on replacement and porosity

generation during experimental dolomitization of limestones. Geochimica et Cosmochimica Acta 303, 137–158. https://doi.org/10.1016/j.gca.2021.03.029.
Whitaker, F.F., Smart, P.L., Jones, G.D., 2004. Dolomitization: from conceptual to numerical models. Geological Society, London, Special Publications 235, 99–139. https://doi.org/10.1144/GSL.SP.2004.235.01.05.
White, W., 2013. Geochemistry, 55 pp.
Xu, L., Marks, B., Toussaint, R., Flekkøy, E.G., Måløy, K.J., 2018. Dispersion in Fractures With Ramified Dissolution Patterns. Front. Phys. 6, 29, 186. https://doi.org/10.3389/fphy.2018.00029.
Yao, S., Gomez-Rivas, E., Martín-Martín, J.D., Gómez-Gras, D., Travé, A., Griera, A., Howell, J.A., 2020. Fault-controlled dolostone geometries in a transgressive–regressive sequence stratigraphic framework. Sedimentology. https://doi.org/10.1111/sed.12739.
Yardley, B.W.D., Rhede, D., Heinrich, W., 2014. Rates of Retrograde Metamorphism and their Implications for the Rheology of the Crust: an Experimental Study. Journal of Petrology 55, 623–641. https://doi.org/10.1093/petrology/egu001.
Yoshida, K., Kuwatani, T., Hirajima, T., Iwamori, H., Akaho, S., 2018. Progressive evolution of whole-rock composition during metamorphism revealed by multivariate statistical analyses. J Metamorph Geol 36, 41–54. https://doi.org/10.1111/jmg.12282.
Zhang, W., Guan, P., Jian, X., Feng, F., Zou, C., 2014. In situ geochemistry of Lower Paleozoic dolomites in the northwestern Tarim basin: Implications for the nature, origin, and evolution of diagenetic fluids. Geochem. Geophys. Geosyst. 15, 2744–2764. https://doi.org/10.1002/2013GC005194.

Figure captions

Fig. 1. Location of the Maestrat Basin (a) and geological map of the study area with an emphasize on the distribution of dolostones in the Benassal Formation (orange) (b, modified from (Martín-Martín et al., 2012)). Studied samples are represented by stars, blue ones being the collected samples and red ones the analysed ones (BEN 10 (dolostone), BEN 4 (dedolomitized rock)). c) Synthetic lithostratigraphic log for the study area (modified from (Gomez-Rivas et al., 2014)).

Fig. 2. Field views of the Benassal Formation from Orpesa de Mar (a) and representation of the stratabound dolostone bodies and the limestone beds location (b). (c) Contact between dolostone and dedolomite rock separated with stylolite (Sample BEN 4, location Fig. 1). Polished slab of representative dolostone (d, Sample BEN 10, location Fig. 1) and dedolomite rock (e, Sample BEN 4, location Fig. 1).

Fig. 3. Backscattered electron image (BSE-SEM) of the replacement of dolomite by calcite with associated phase map obtained from greyscale segmentation (Sample BEN 4, see location in Fig. 1).

Fig. 4. Sample located in the partially dedolomitized rock (a). Phase map (b) with associated Zn (c), Sr (d), La (e) and U (f) in calcite. To represent the calcite, maps were calibrated using Ca as internal standard. Note that the colour scale is logarithmic (μg/g). Pixel size 17 × 17 μm. Maps are plotted via XMapTools 4 (Lanari et al., 2014, 2019).

Fig. 5. Average chemical composition of calcite and dolomite from the original limestone and dolostone respectively (Centrella et al., 2023), and the calcite from dedolomite (sample BEN 4A & B). All the compositions are normalized to world shale (Piper, 1974) and come from average chemical composition obtained from quantitative trace element maps.

Fig. 6. EBSD data on dolomite-calcite transition with respective lower hemisphere equal area projection. Note that for a), lower hemispheres are for the entire map whereas b), local domain within

the map. Colour code are equal between maps and lower hemispheres equal projection. For more visibility, analysed pixels are surrounded with dashed circle. Sample BEN 4A (a) and B (b).

Fig. 7. Mass transfer diagram for the dolomite-calcite replacement using the data obtained from the Gresens analysis (Gresens, 1967). Elements are organized using a scaling approach.

Fig. 8. Sketch illustrating a conceptual model for the dedolomitization of the Benassal Formation. Fluid infiltration through the major fault (Benassal Formation scale) with percolation of the fluid through the dolostone (Rock scale). Simultaneous dissolution of the MVT and dolostone and precipitation of the calcite. At the fluid-minerals interfaces, Zn, Mn, Rb, Ca and LREE are gained, and Fe, Mg, U, Sr and HREE are lost.

Table 1. Microprobe analyses of dolomite and calcite. Modified from (Centrella et al., 2023).

Empty Cell	Dolostone				Dedolomite					
	Dolomite (Sample BEN10)				Dolomite		Empty Cell	Calcite		
Analysis	3	9	10	Avg.	Ben4B-3	Ben4B-7		BEN4B-14	BEN4A-5	Avg.
Fe	0.86	1.05	1.30	1.08	0.90	1.28		0.04	0.02	0.02
Mn	0.05	0.00	0.00	0.02	0.11	0.02		0.02	0.00	0.04
Mg	11.74	11.83	11.89	11.75	11.62	11.62		0.34	0.37	0.38
Ca	21.71	21.32	21.18	21.51	21.82	20.91		38.86	38.77	39.88
Normalized to 2 oxygens										
Fe	0.030	0.036	0.045	0.037	0.031	0.045		0.001	0.001	0.001
Mn	0.002	0.000	0.000	0.001	0.004	0.001		0.001	0.000	0.001
Mg	0.928	0.938	0.940	0.930	0.919	0.934		0.029	0.031	0.031
Ca	1.041	1.026	1.016	1.032	1.046	1.020		1.969	1.968	1.967
Sum	2.000	2.000	2.000	2.000	2.000	2.000		2.000	2.000	2.000
XDol.	0.97	0.96	0.95	0.96	0.96	0.95	XCal.	0.98	0.98	0.98
XAnk.	0.03	0.04	0.05	0.04	0.03	0.05	XMag.	0.01	0.02	0.02
XKut.	0.00	0.00	0.00	0.00	0.00	0.00	XSid.	0.00	0.00	0.00
							XRho.	0.00	0.00	0.00
Density (g.cm-3)	2.85	2.85	2.85	2.85	2.85	2.85		2.72	2.72	2.72

Table 2. Average major and trace element composition of dolomite ((Centrella et al., 2023) and calcite obtained with XMapTools 4 (Lanari et al., 2014, 2019). Results of the mass-balance equation are presented in grams from a solid volume variation of +5%. Elements with negative values are lost during dedolomitization whereas positive ones are gained.

Major element (wt.%)	Dolostone Dolomite			Calcite			Mass balance
	Avg.	BEN 4A	BEN 4B	Avg.	BEN 4A	BEN 4B	Avg.	Mass change (grams)
Fe	1.08	0.79	1.08	0.94	0.04	0.02	0.02	−1.054
Mn	0.02	0.01	0.02	0.02	0.02	0.00	0.04	0.021
Mg	11.75	12.79	11.92	12.35	0.34	0.37	0.38	−11.374
Ca	21.51	21.65	21.28	21.47	38.77	38.86	39.88	18.459
C	13.37	12.94	13.38	13.16	11.86	12.27	11.86	−1.481
Trace element (μg/g)								
V	4.016	6.811	6.695	4.703	3.285	3.498	3.392	−6.18E-05
Zn	24.634	32.364	17.508	19.046	72.977	49.048	61.013	3.65E-03
Rb	1.030	0.213	0.235	1.069	1.587	1.520	1.553	5.27E-05
Sr	25.570	21.090	22.524	21.398	15.585	12.757	14.171	−1.14E-03
Y	3.190	1.832	1.723	1.433	2.720	2.386	2.553	−6.32E-05
La	1.659	1.010	0.984	1.037	1.872	1.914	1.893	2.37E-05
Ce	1.923	1.670	1.460	1.406	2.054	2.050	2.052	1.33E-05
Pr	0.321	0.238	0.229	0.211	0.380	0.377	0.378	5.85E-06
Nd	1.349	0.986	0.939	0.867	1.568	1.578	1.573	2.27E-05
Sm	0.767	0.581	0.565	0.504	0.934	0.914	0.924	1.59E-05
Eu	0.063	0.052	0.050	0.042	0.077	0.074	0.076	1.29E-06
Gd	0.344	0.251	0.247	0.201	0.383	0.365	0.374	2.99E-06
Tb	0.050	0.039	0.038	0.029	0.054	0.048	0.051	6.39E-08
Dy	0.334	0.249	0.246	0.178	0.336	0.285	0.311	−2.25E-06
Ho	0.076	0.052	0.052	0.038	0.071	0.056	0.064	−1.19E-06
Er	0.227	0.154	0.154	0.109	0.202	0.160	0.181	−4.56E-06
Tm	0.031	0.020	0.020	0.014	0.026	0.021	0.023	−7.27E-07
Yb	0.184	0.129	0.119	0.087	0.159	0.121	0.140	−4.39E-06
Lu	0.030	0.018	0.017	0.013	0.026	0.023	0.025	−5.57E-07
Pb	1.569	0.245	0.449	0.658	1.366	1.711	1.538	−2.79E-06
U	0.530	0.303	0.353	0.528	0.313	0.258	0.286	−2.44E-05

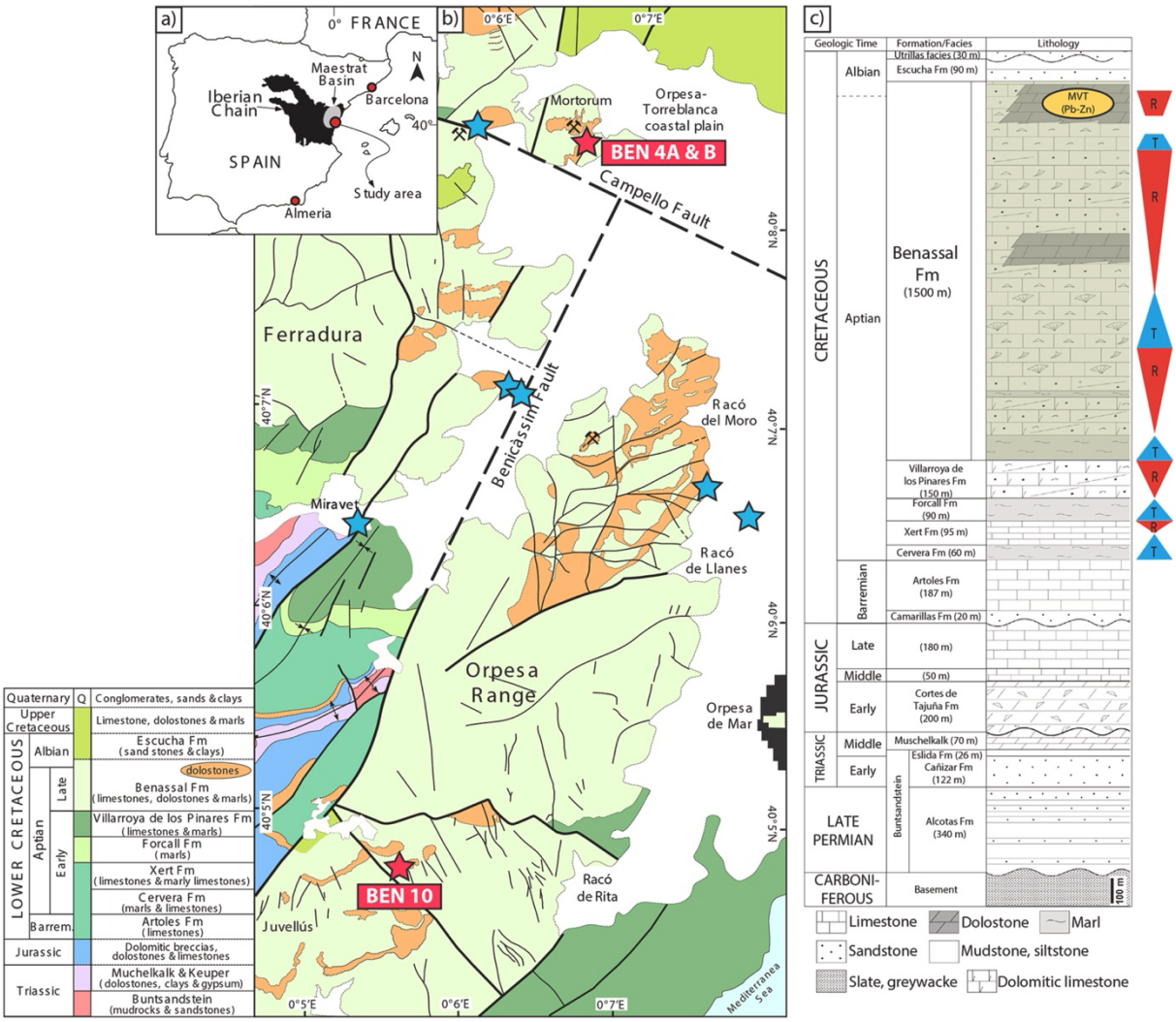
a)
0° FRANCE
Maestrat Basin
Iberian Chain
Barcelona
40°
SPAIN
Study area
Almeria
b)
0°6'E
0°7'E
Mortorum
Orpesa-Torreblanca coastal plain
BEN 4A & B
Campello Fault
40°8'N
Ferradura
Benicassim Fault
40°7'N
Racó del Moro
Miravet
Racó de Llanes
40°6'N
40°5'N
Orpesa Range
Orpesa de Mar
BEN 10
Racó de Rita
Juvellús
Mediterranea Sea
Quaternary
Q
Conglomerates, sands & clays
Upper Cretaceous
Limestone, dolostones & marls
LOWER CRETACEOUS
Albian
Escucha Fm (sand stones & clays)
Aptian
Late
dolostones
Benassal Fm (limestones, dolostones & marls)
Early
Villarroya de los Pinares Fm (limestones & marls)
Forcall Fm (marls)
Xert Fm (limestones & marly limestones)
Cervera Fm (marls & limestones)
Barrem.
Artoles Fm (limestones)
Jurassic
Dolomitic breccias, dolostones & limestones
Triassic
Muschelkalk & Keuper (dolostones, clays & gypsum)
Buntsandstein (mudrocks & sandstones)
c)
Geologic Time
Formation/Facies
Lithology
CRETACEOUS
Albian
Utrillas facies (30 m)
Escucha Fm (90 m)
MVT (Pb-Zn)
Aptian
Benassal Fm (1500 m)
Villarroya de los Pinares Fm (150 m)
Forcall Fm (90 m)
Xert Fm (95 m)
Cervera Fm (60 m)
Barremian
Artoles Fm (187 m)
Camarillas Fm (20 m)
JURASSIC
Late
(180 m)
Middle
(50 m)
Early
Cortes de Tajuña Fm (200 m)
TRIASSIC
Middle
Muschelkalk (70 m)
Early
Buntsandstein
Eslida Fm (26 m)
Cañizar Fm (122 m)
LATE PERMIAN
Alcotas Fm (340 m)
CARBONI-FEROUS
Basement
100 m
R
T
Limestone
Dolostone
Marl
Sandstone
Mudstone, siltstone
Slate, greywacke
Dolomitic limestone

Figure 1

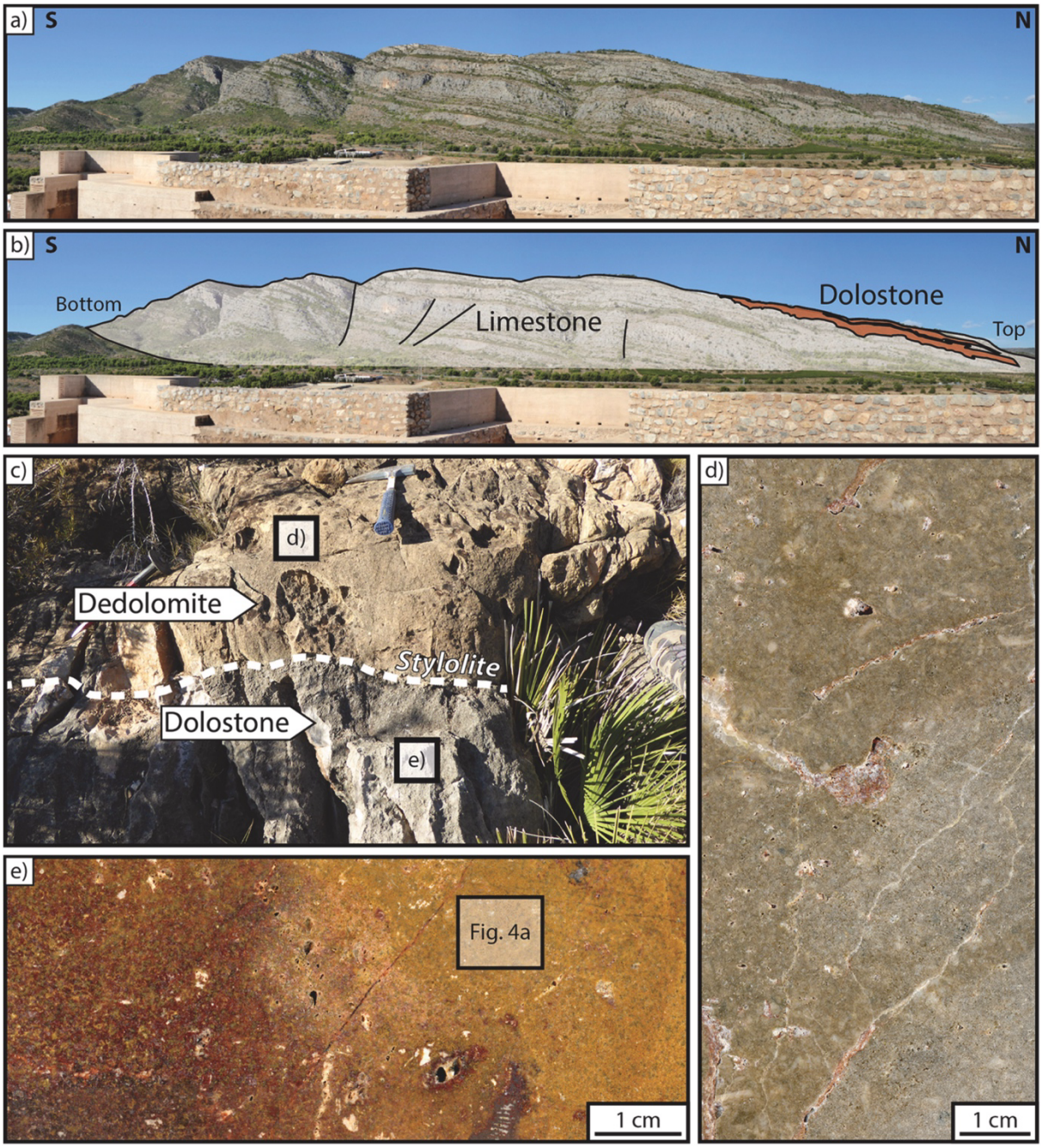
a)
S
N
b)
S
N
Bottom
Limestone
Dolostone
Top
c)
d)
Dedolomite
Stylolite
Dolostone
e)
d)
e)
Fig. 4a
1 cm
1 cm

Figure 2

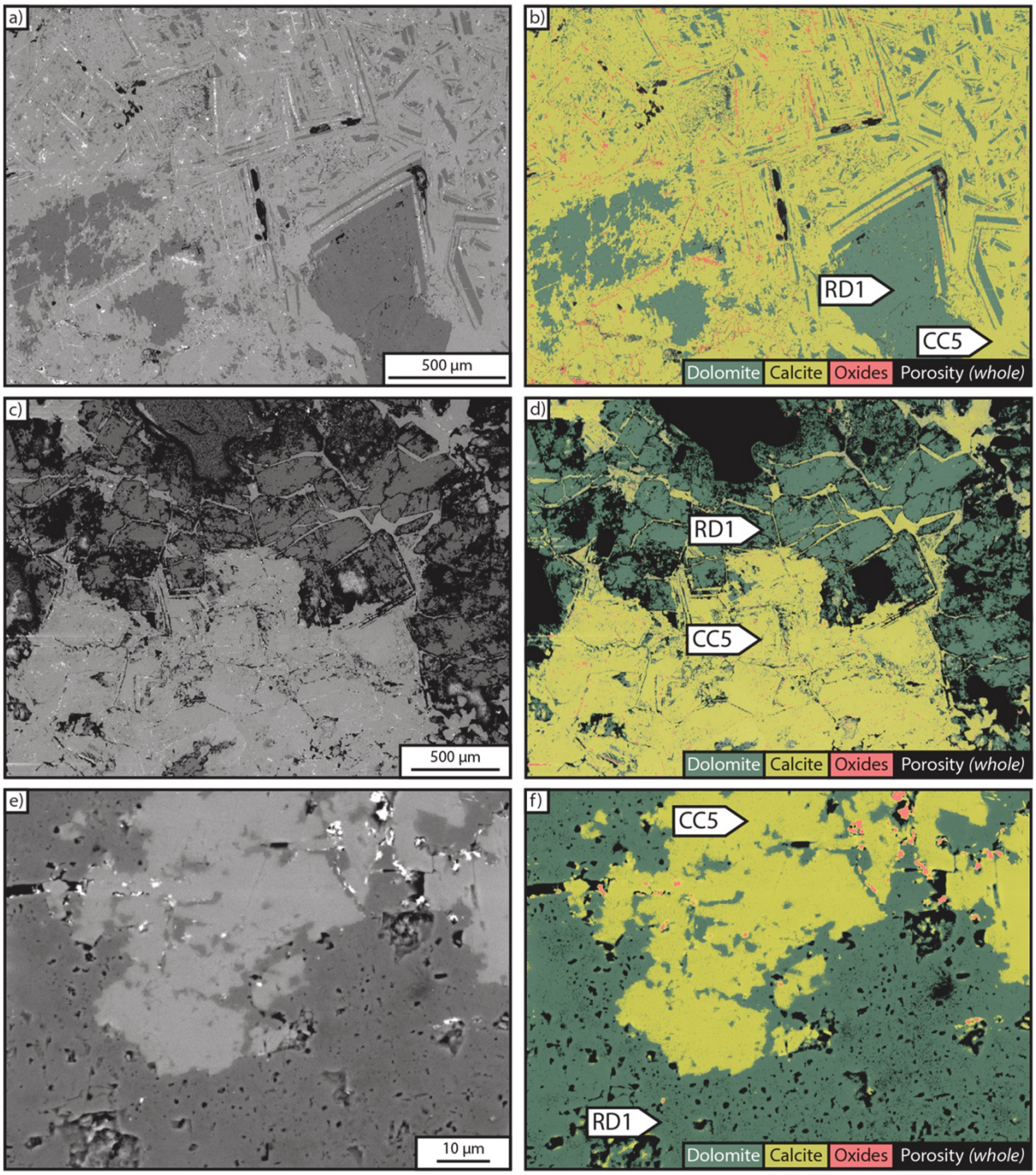
a)
500 µm
b)
RD1
CC5
Dolomite
Calcite
Oxides
Porosity (whole)
c)
500 µm
d)
RD1
CC5
Dolomite
Calcite
Oxides
Porosity (whole)
e)
10 µm
f)
CC5
RD1
Dolomite
Calcite
Oxides
Porosity (whole)

Figure 3

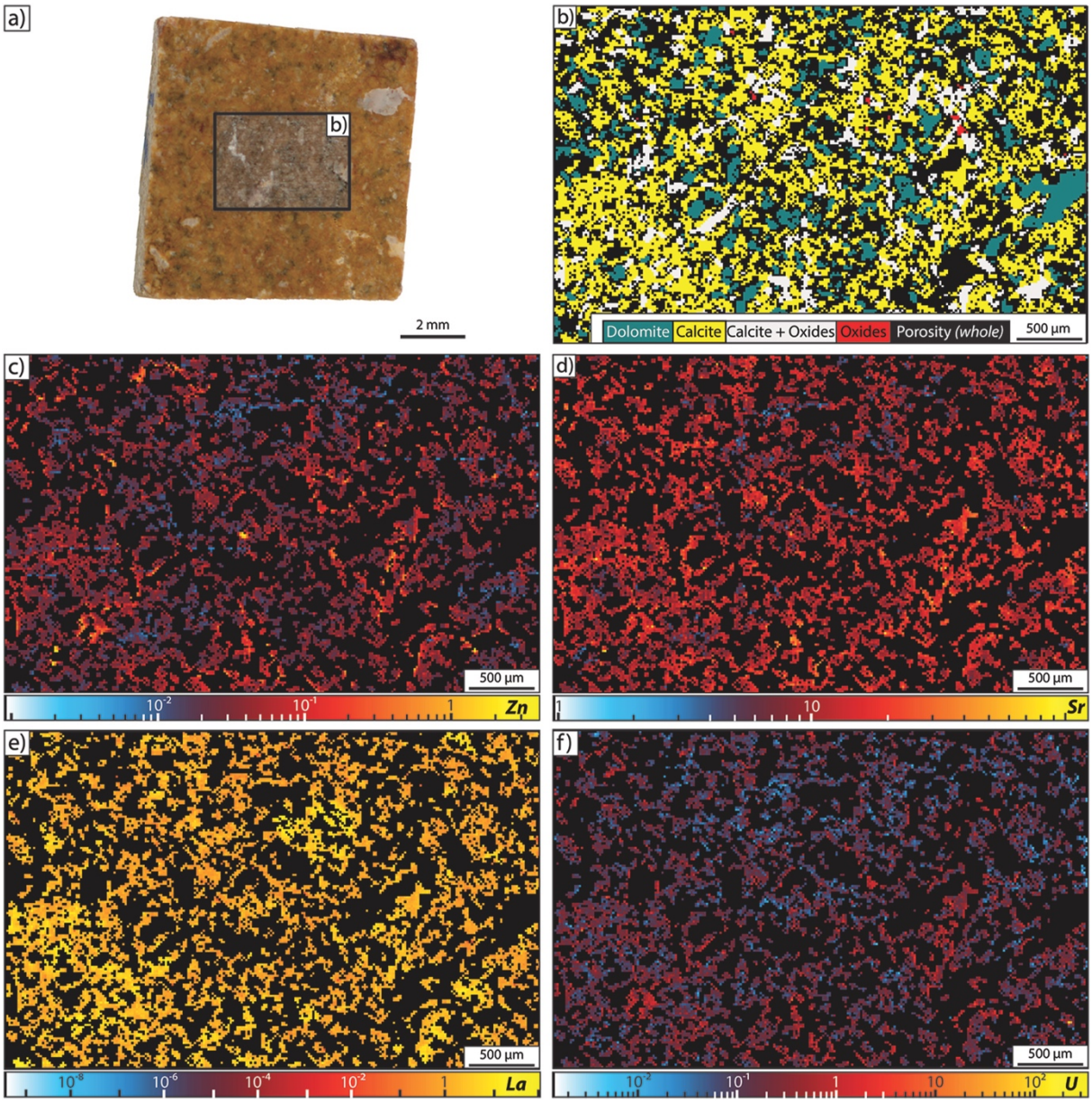
a)
b)
2 mm
b)
Dolomite
Calcite
Calcite + Oxides
Oxides
Porosity (whole)
500 µm
c)
500 µm
10-2
10-1
1
Zn
d)
500 µm
1
10
Sr
e)
500 µm
10-8
10-6
10-4
10-2
1
La
f)
500 µm
10-2
10-1
1
10
102
U

Figure 4

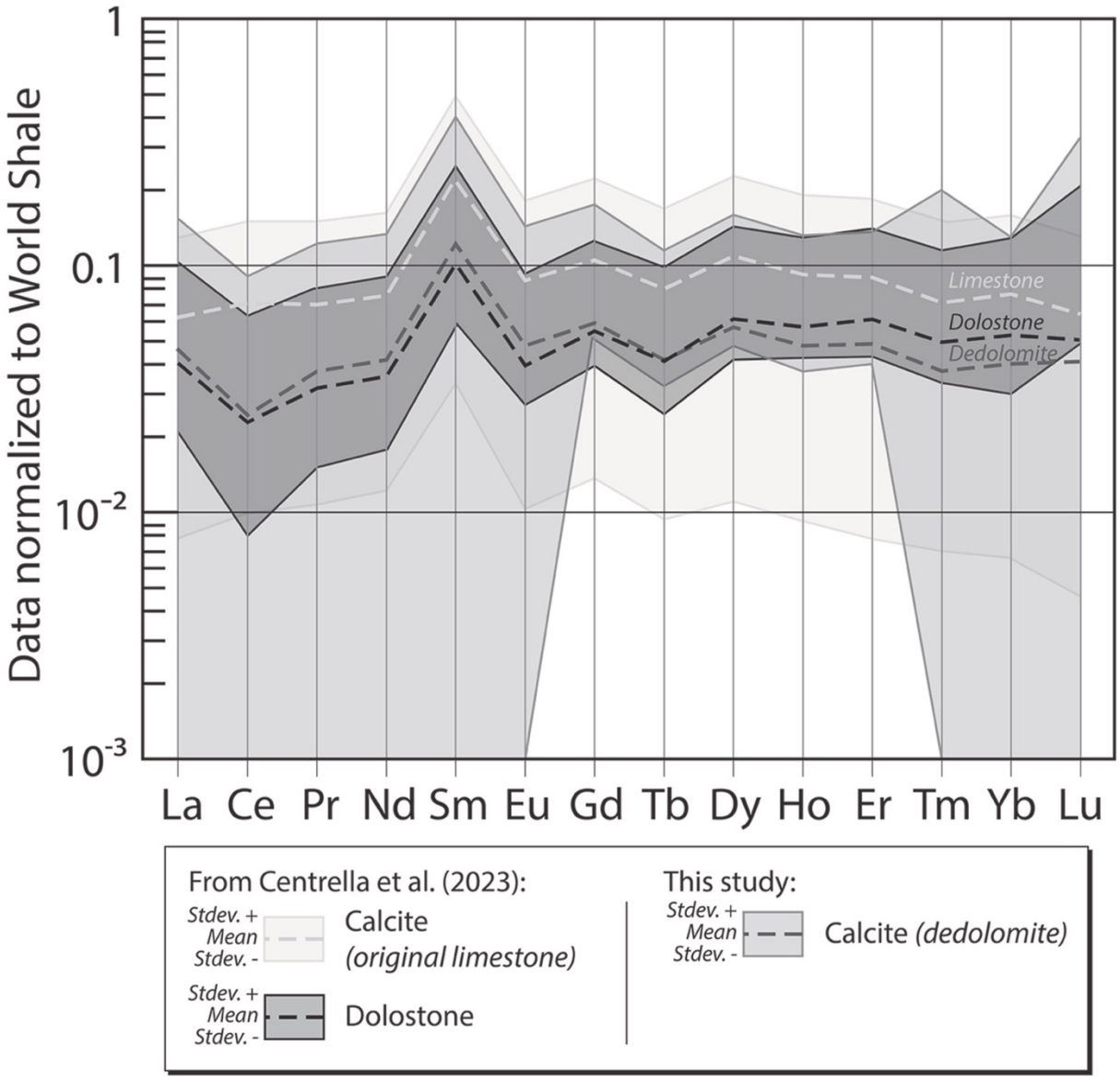
Data normalized to World Shale
1
0.1
10-2
10-3
La Ce Pr Nd Sm Eu Gd Tb Dy Ho Er Tm Yb Lu
Limestone
Dolostone
Dedolomite
From Centrella et al. (2023):
Stdev. +
Mean
Stdev. -
Calcite
(original limestone)
Stdev. +
Mean
Stdev. -
Dolostone
This study:
Stdev. +
Mean
Stdev. -
Calcite (dedolomite)

Figure 5

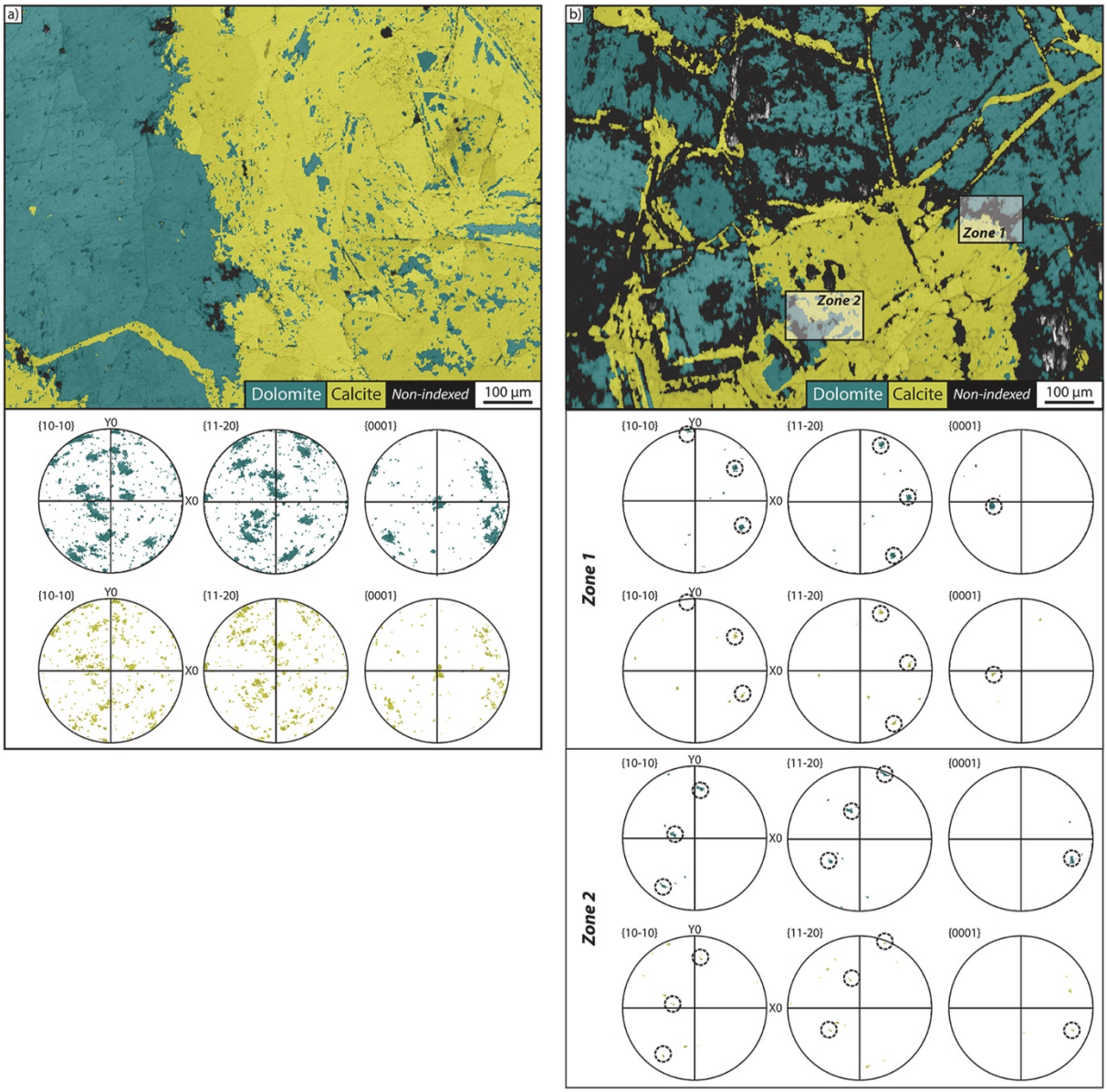
a)
Dolomite
Calcite
Non-indexed
100 µm
{10-10}
Y0
X0
{11-20}
{0001}
b)
Zone 1
Zone 2
Dolomite
Calcite
Non-indexed
100 µm
Zone 1
Zone 2

Figure 6

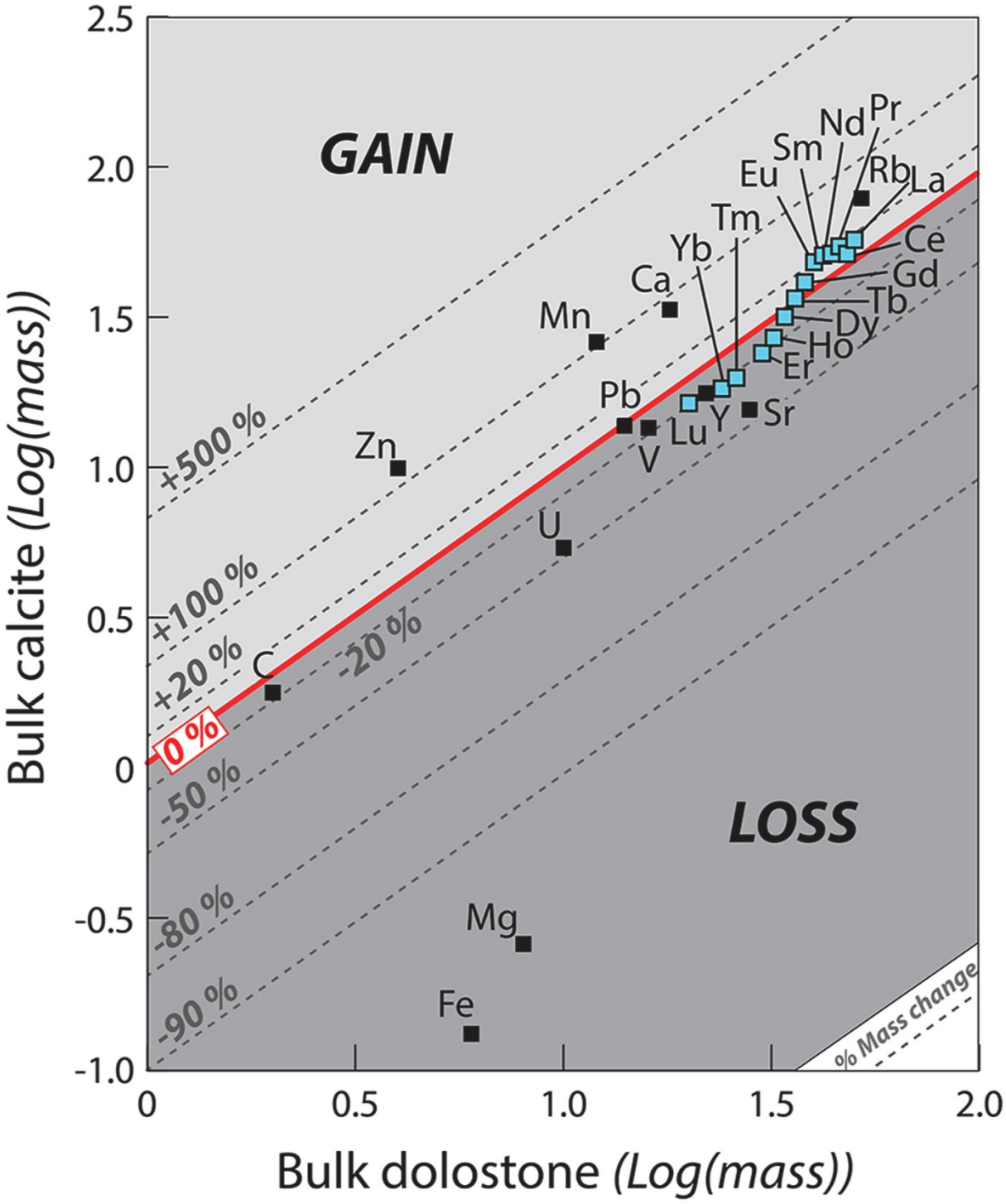
GAIN
LOSS
Bulk calcite (Log(mass))
Bulk dolostone (Log(mass))
2.5
2.0
1.5
1.0
0.5
0
-0.5
-1.0
0
0.5
1.0
1.5
2.0
+500 %
+100 %
+20 %
0 %
-20 %
-50 %
-80 %
-90 %
% Mass change
Nd
Pr
Sm
Eu
Rb
La
Tm
Yb
Ce
Ca
Gd
Mn
Tb
Dy
Ho
Er
Pb
Y
Sr
Lu
V
Zn
U
C
Mg
Fe

Figure 7

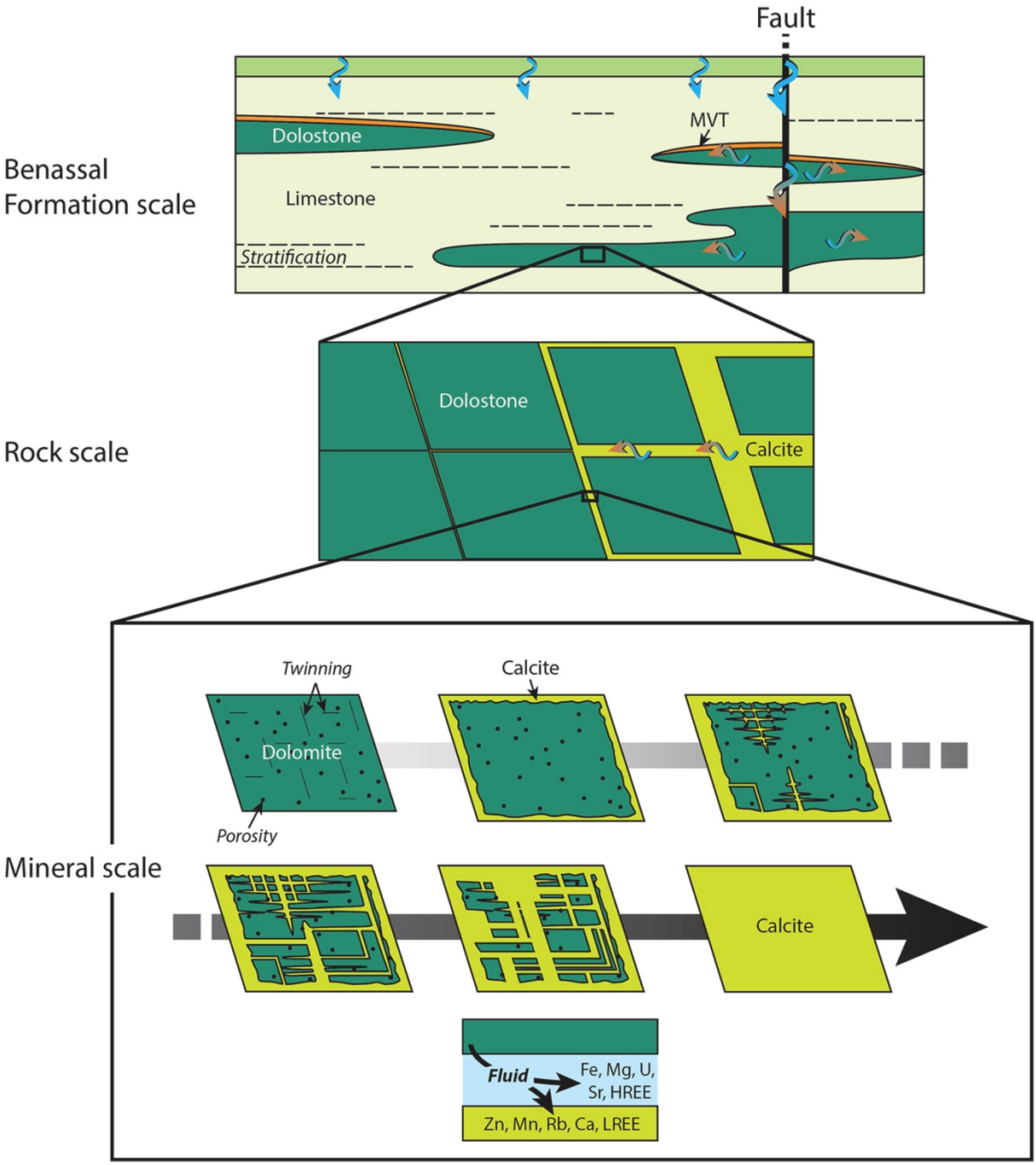
Fault
Benassal
Formation scale
Dolostone
MVT
Limestone
Stratification
Rock scale
Dolostone
Calcite
Twinning
Calcite
Dolomite
Porosity
Mineral scale
Calcite
Fluid
Fe, Mg, U,
Sr, HREE
Zn, Mn, Rb, Ca, LREE

Figure 8